Journal of Offshore Mechanics and Arctic Engineering. Received March 04, 2022;
Accepted manuscript posted June 27, 2022. doi:10.1115/1.4055281

Three-dimensional Large Eddy Simulations and Proper Orthogonal Decomposition Analysis of Flow around a Flexibly Supported Circular Cylinder

Marek Jan Janocha[a], Lukas Philip Fabricius[a], Guang Yin[a1], Muk Chen Ong[a]

[a]Department of Mechanical and Structural Engineering and Materials Science, University of Stavanger
Stavanger, Norway

Abstract

Three-dimensional (3D) numerical simulations of the flow around a cylinder undergoing vortex-induced vibration (VIV) at Re=3900 (defined as $Re=U_\infty D/\nu$, where U_∞ is the inlet flow velocity, D is the diameter of the cylinder and ν is the fluid kinematic viscosity) are performed using Large Eddy Simulations (LES). Detailed mesh and time-step convergence studies are carried out for the flow past a stationary cylinder to obtain the optimal mesh and time step. The validation studies are performed by comparing the present results with the previous published experimental data and numerical results to confirm feasibility of the present numerical model for predicting the wake characteristics. The numerical model is then applied to investigate the flow around a self-excited cylinder vibrating in the cross-flow direction at three different reduced velocity. The effects of the reduced velocity are analyzed based on the cross-flow vibration amplitudes, the power spectral densities of lift and drag coefficients and the wake flow coherent structures. Different vortex shedding modes are identified and categorized using the iso-surfaces of the pressure coefficient and the Q-criterion. The dominant 3D wake flow features are extracted and discussed by carrying out the Proper Orthogonal Decomposition (POD) for flow velocities on multiple two-dimensional (2D) sampling planes in the wake region. The modes on the XY planes display a traveling-wave behavior and the modes on the XZ planes shows cells of streamwise vortices, which displays the three-dimensionality of the wake flow.

Keywords: 3D Large Eddy Simulation; vortex-induced vibration; Proper Orthogonal Decomposition

1. Introduction

The phenomenon of vortex induced vibration has been a core interest of fluid-structure-interaction (FSI) studies for many years. Feng [1] performed an experiment of a cylinder in air and was the first to perform detailed measurements of vortex-induced vibration and discovered the lock-in phenomenon. Sumer and Fredsøe [2] have given an extensive description of flow around circular cylinders. Numerous studies have investigated the effects of physical parameters such as the mass ratio m^* (defined as the ratio of the cylinder mass and the mass of the displaced fluid) and the number of DoF on the VIV behavior. Jauvtis and Williamson [3] showed that for a cylinder free to respond in 2DoF the mass ratio has a significant effect on the vortex shedding dynamics. A new vortex shedding mode named a 2T mode occurring for m^* lower than 6 was observed. Assi et al. [4] performed experiments for cylinders vibrating in 1DoF (cross-flow direction) and a m^* of 0.96 and 0.90, they reported maximum displacements of

[1] Corresponding author: guang.yin@uis.no

Journal of Offshore Mechanics and Arctic Engineering. Received March 04, 2022;
Accepted manuscript posted June 27, 2022. doi:10.1115/1.4055281

approximately 2 times the cylinder diameter ($2D$). Govardhan and Williamson [5] found a critical $m^* = 0.54$ based on their observations where the cross-flow amplitude response for experiments with $m^* \leq 0.54$ was increased dramatically.

Numerical simulations have also been used to study the vortex induced vibration. Due to the complexity of fluid-structure-interaction and the wake flow dynamics, most of the numerical simulations were carried out at low Reynolds numbers such as Griffith et al. [6], Zhao and Yan [7], Zhao et al. [8]. For high Reynolds number flows, Reynolds-Averaged Navier-Stokes simulations (RANS) are usually used, such as Wu et al. [9], Janocha et al. [10], Serta et al. [11]. Recent increase of computational power has made scale-resolved three-dimensional numerical simulations of the VIV phenomenon possible. The objective of the present study is to investigate the three-dimensional wake flow behavior behind a vibrating cylinder using 3D Large Eddy Simulations (LES).

Since VIV can result in drag amplification and fatigue, the mitigation of VIV is of great interest. To develop VIV mitigation strategies, comprehensive knowledge of the flow structures around a cylinder undergoing VIV is of great interest. The coherent flow structures are temporally and spatially correlated flow patterns, and they dominate the main flow dynamics. To extract these energetic flow motions, the modal decomposition analysis is often adopted to decompose the flow field into a series of coherent flow structures. For example, Riches et al. [12] have used Proper Orthogonal Decomposition (POD) on experimental data to analyze the wake-dynamics of a low mass-ratio ($m^* = 5.3$) circular cylinder. They have found that for the initial branch 6 POD modes are required to capture the salient aspects of the flow while in the upper branch 7 modes are required. The dynamic mode decomposition (DMD) and POD are used by Janocha et al. [13] to analyze the coherent structures of flow around vibrating isolated and piggyback cylinders configurations subjected to a uniform flow at a laminar Reynolds number and an upper transition Reynolds number. The 2D numerical simulations were performed to obtain the snapshots for the modal decomposition analysis. To the authors' best knowledge, there are only a few published studies that applied the POD analysis to investigate the flow around moving bodies. Among these studies none of them was focused on investigating the spanwise variance of the mode's spatial structures. Most of the available published studies are using either a phase averaged experimental data, or a 2D flow field data obtained from numerical simulations to formulate the snapshot matrix for the POD analysis. In the present paper, the modal decomposition is applied to the 3D flow field in the cylinder wake region. To decrease the memory requirements, data snapshots comprising three velocity components are gathered on multiple two-dimensional (2D) sampling planes in the wake region

The paper is organized as follows. Section 2 gives a brief introduction to the numerical method used in the present study. Section 3 introduces the computational overview. Section 4 gives the results and discussion. Finally, the conclusion is made in Section 5.

Journal of Offshore Mechanics and Arctic Engineering. Received March 04, 2022;
Accepted manuscript posted June 27, 2022. doi:10.1115/1.4055281

2. Materials and methods

2.1 Governing equations

The governing equations of the present study are the incompressible filtered Navier Stokes equations for Large Eddy Simulations (LES) given as

$$\frac{\partial \bar{u}_i}{\partial x_i} = 0, \tag{1}$$

$$\frac{\partial \bar{u}_i}{\partial t} + \frac{\partial (\bar{u}_i \bar{u}_j)}{\partial x_j} = -\frac{1 \partial \bar{p}}{\rho \partial x_i} + \nu \frac{\partial^2 \bar{u}_i}{\partial {x_j}^2} - \frac{\partial \tau_{ij}}{\partial x_j}, \tag{2}$$

where $\overline{u_\iota}, i \in [1,2,3]$ is the filtered velocity, ρ is the density of the fluid, $\bar{p}$ is the filtered pressure and τ_{ij} is the unresolvable sub-grid stress. The sub-grid stress is given by equation.

$$\tau_{ij} = \overline{u_\iota u_j} - \overline{u_\iota}\,\overline{u_j} \tag{3}$$

where the overbar denotes the filtering. In the present study, the Wall-adapting Local Eddy-viscosity (WALE) sub-grid stress model (Nicoud and Ducros [14]) is selected to resolve the sub-grid stress. The sub-grid model is based on the squared velocity gradient tensor, and it takes the shear stress and rotation tensor into consideration. The turbulent eddy viscosity ν_t is given by

$$\nu_t = (c_\omega \Delta)^2 \frac{(s_{ij}^d s_{ij}^d)^{3/2}}{(\bar{S}_{ij}\bar{S}_{ij})^{5/2} + (s_{ij}^d s_{ij}^d)^{5/4}}, \tag{4}$$

where

$$\bar{S}_{ij} = \frac{1}{2}\left(\frac{\partial \bar{u}_i}{\partial x_j} + \frac{\partial \bar{u}_j}{\partial x_i}\right), \tag{5}$$

and

$$s_{ij}^d = \bar{S}_{ik}\bar{S}_{kj} + \bar{\Omega}_{ik}\bar{\Omega}_{kj} - \frac{1}{3}\delta_{ij}[\bar{S}_{mn}\bar{S}_{mn} - \bar{\Omega}_{mn}\bar{\Omega}_{mn}]. \tag{6}$$

In these equations, $\bar{S}_{ij}$ is the strain rate tensor and $\bar{\Omega}_{ik}$ is the rotation rate tensor.

The present simulations consider a rigid cylinder that is elastically supported by a spring-damper system. The cylinder is free to move in the cross-flow direction which can be modeled as a 1 DoF system. The equation of the motion in the cross-flow direction is given as:

$$U_r^2 \frac{\partial^2 y}{\partial t^2} + 4\pi\zeta U_r \frac{\partial y}{\partial t} + 4\pi^2 x = \frac{2U_r^2 C_L}{\pi m^*}, \tag{7}$$

where y denotes the dimensionless cross-flow displacements, U_r is the reduced velocity and ζ is the damping ratio. C_L is the lift coefficient. The mass-ratio is given by

$$m^* = \frac{m}{m_d} \tag{8}$$

where m is the mass of the cylinder and m_d is the displaced mass. The structural damping ratio is given by:

$$\zeta = \frac{c}{2\sqrt{km}} \tag{9}$$

where c is the structural damping and k is the structural stiffness.

The governing equations are solved using the open-source finite volume CFD code OpenFOAM [15]. The PIMPLE algorithm which combines the Pressure-Implicit Split-Operator (PISO) and the Semi-Implicit Method for Pressure-Linked Equations (SIMPLE) is applied to solve the pressure-velocity coupling. The time discretization is conducted using the second order implicit backwards scheme. The spatial discretization is based on the second order Gauss linear scheme. Therefore, the overall method is of second order accuracy. The Geometric Agglomerated Algebraic Multigrid (GAMG) solver with a residual level set to 10^{-6} is used to solve the pressure equation. The Preconditioned Bi-Conjugate Gradient (PBiCG) solver with a Diagonal Incomplete Lower Upper (DILU) preconditioner with a residual level set to 10^{-8} is used for the momentum equation solution. Five outer corrector loops are used in which the entire system of equations is solved within one time step. In each of the outer corrector loops, there are two corrector (PISO) loops solving the pressure equation and the momentum corrector equation.

2.2 Computational domain and boundary conditions

The size of the computational domain, as shown in Fig. 1, is $(L_x, L_y, L_z)/D = (40,20,4)$. According to Prsic et al. [16] where extensive simulations were performed for the flow around stationary smooth cylinders in the subcritical regime, a domain size of at least $4D$ in the spanwise direction is required to properly resolve the spanwise velocity fluctuations. Therefore, in the present simulations the domain is chosen to be $4D$ in the spanwise direction. The boundary conditions used in the present simulations are set as following: a uniform flow profile with $u_x = U_\infty, u_y = 0$ and $u_z = 0$ is used at the inlet and the pressure is prescribed as zero normal gradient; A no-slip boundary condition is applied on the cylinder surface with $u_x = u_y = u_z = 0$; The upper and lower boundaries are specified with zero normal gradients for the velocities and the pressure; In the spanwise direction, a cyclic boundary condition is imposed at the front and back boundaries; At the outlet, a reference pressure is set to be $p = 0$ and the velocities are prescribed as zero normal gradient.

Journal of Offshore Mechanics and Arctic Engineering. Received March 04, 2022;
Accepted manuscript posted June 27, 2022. doi:10.1115/1.4055281

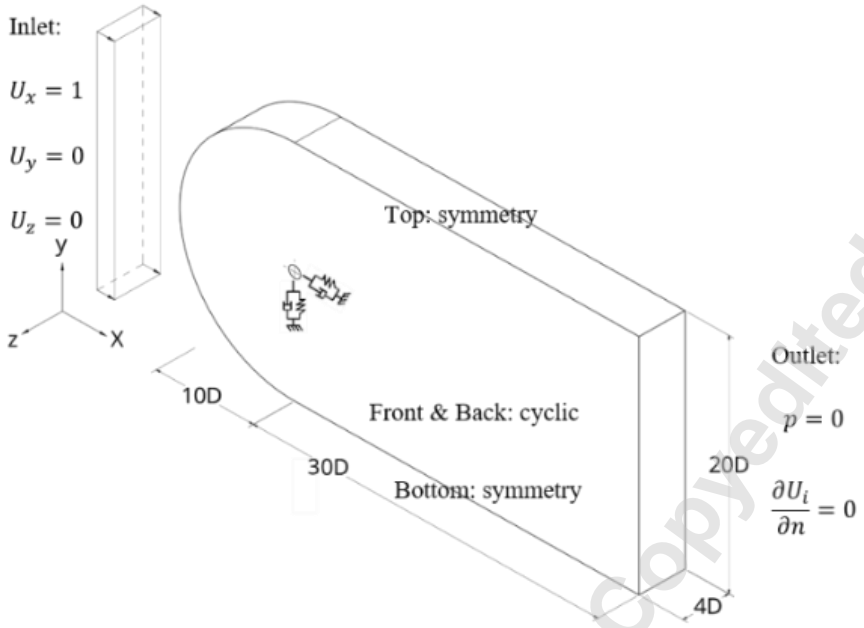

FIGURE 1: Schematic of the computational domain with imposed boundary conditions.

3. Results and discussion

3.1 Mesh and time-step convergence studies and validation studies

The accuracy of LES simulations is highly dependent on the computational grid density and quality of computational cells. The computational grid topology in the *x*-*y* plane used in present simulations is showed in Fig. 2. The circular zone around the cylinder is generated by radial extrusion of quadrilateral cells with a constant stretching factor 1.05. Downstream the cylinder, the cells are clustered in the wake region. Away from the wake region, the cells are progressively stretched to decrease the overall cell number to reduce the computational cost. Grid in the spanwise direction (z-axis) is generated by extruding the 2D grid shown in Fig 2 with equidistant grids.

Journal of Offshore Mechanics and Arctic Engineering. Received March 04, 2022;
Accepted manuscript posted June 27, 2022. doi:10.1115/1.4055281

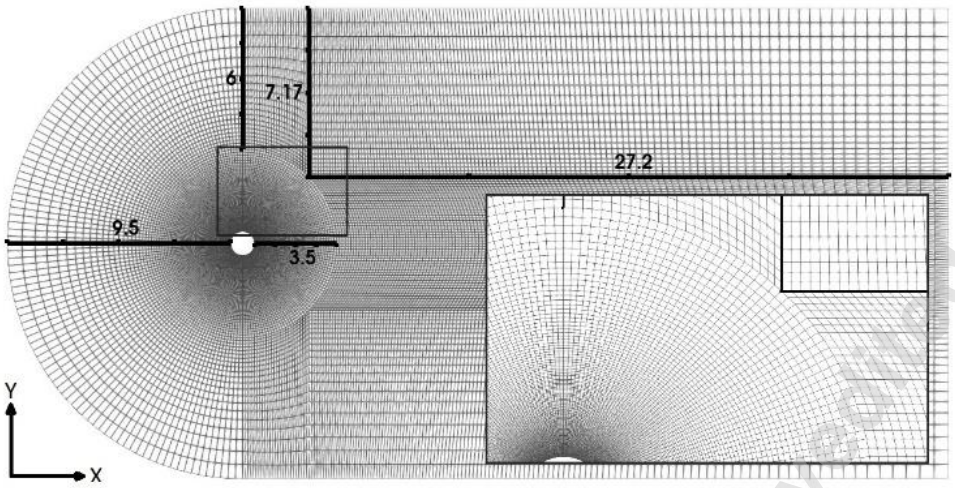

FIGURE 2: A Computational grid overview in the x-y plane, dimensions given in terms of cylinder diameter (D). In the spanwise (z-axis) direction the grid is formed by extruding the presented 2D grid using a uniform spacing.

A mesh sensitivity study is performed to make sure that the results are independent of the mesh size. Three simulations of a static cylinder with different mesh resolutions are performed. To evaluate the influence of the mesh size on the results, representative hydrodynamic quantities are compared. The cell number for each mesh is 2636296, 5031296 and 9935520, respectively. The mesh resolution is refined with a constant refinement factor. The grid convergence for the values of $\overline{C_D}$ (defined as $C_D = F_x/(0.5U_\infty^2 DL_z)$ where is the force acting on the cylinder in the streamwise direction), C_L^{rms} and St (defined as $St = f_v D/U$ where f_v is the frequency of vortex shedding) is shown in Fig. 3. The spanwise grid number of the three cases are 48, 64 and 80, respectively. The height of the first cell close to the cylinder surface is set to be $0.001D$, which is close the value used by Tian & Xiao [17]. The value of $\overline{C_D}$ is relatively insensitive to mesh refinement and the relative error between the cases with the normal and fine mesh is smaller than 5%. The C_L^{rms} shows larger variation and is sensitive to mesh resolution. The large differences between the obtained C_L^{rms} values can be partially attributed to the random nature of the turbulent fluctuations in the separated shear layers. Fig. 4 shows the skin friction factor (C_f defined as $C_f = \tau_w/(0.5U_\infty^2 DL_z)$ where τ_w is the wall shear stress on the surface) distribution on the cylinder surface. The simulations with normal and fine meshes predict the same C_f distribution on the cylinder's surface. It can be concluded that for the fine and normal mesh cases, the differences between $\overline{C_D}$ and St are smaller than 1% and the predicted separation angles are nearly identical. More detailed mesh convergence studies in terms of can be found in Janocha et al. [18]. The results obtained in the mesh sensitivity study show a clear convergent behavior when increasing mesh refinement and are in support for selecting the normal mesh variant for further computations which provides a good balance of computational cost and accuracy.

Journal of Offshore Mechanics and Arctic Engineering. Received March 04, 2022;
Accepted manuscript posted June 27, 2022. doi:10.1115/1.4055281

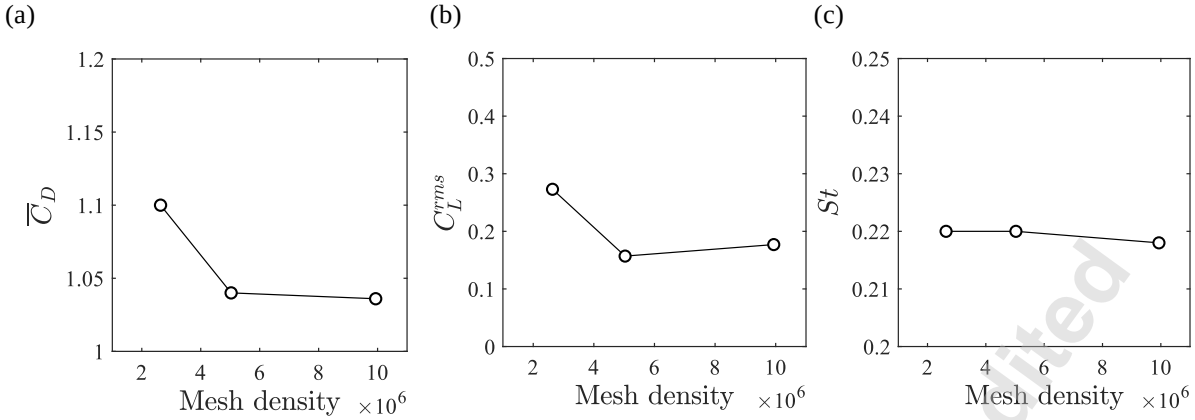

FIGURE 3: The grid convergence study results for: (a) $\overline{C_D}$; (b) C_L^{rms}; (c) St.

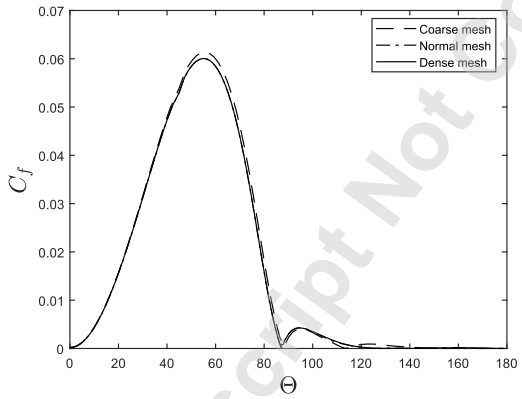

FIGURE 4: The absolute value of the time- and spanwise-averaged skin friction coefficient (C_f) on the cylinder surface for different mesh variants.

Three additional simulations with different time steps are performed to obtain a result that is independent of the time step size. Fig. 5 shows the resulting representative hydrodynamic quantities for different time step sizes of $\Delta t U_\infty/D = 0.002, 0.001$ and 0.0005. The normal density mesh variant (with a cell number of 5031296) is used in time step sensitivity study. The max Courant number is below 1 for all simulation cases. The differences between the hydrodynamic quantities of the investigated cases are small with a relative difference of maximum 1.8% for $\overline{C_D}$ and 1% for St. A large variation in the C_L^{rms} is observed due to the stochastic variation of the lift force and not the difference in the time step. Based on the results of time step sensitivity study, a time step $\Delta t U_\infty/D = 0.002$ is considered to be sufficient and is selected for the remaining simulations presented in this paper.

Journal of Offshore Mechanics and Arctic Engineering. Received March 04, 2022;
Accepted manuscript posted June 27, 2022. doi:10.1115/1.4055281

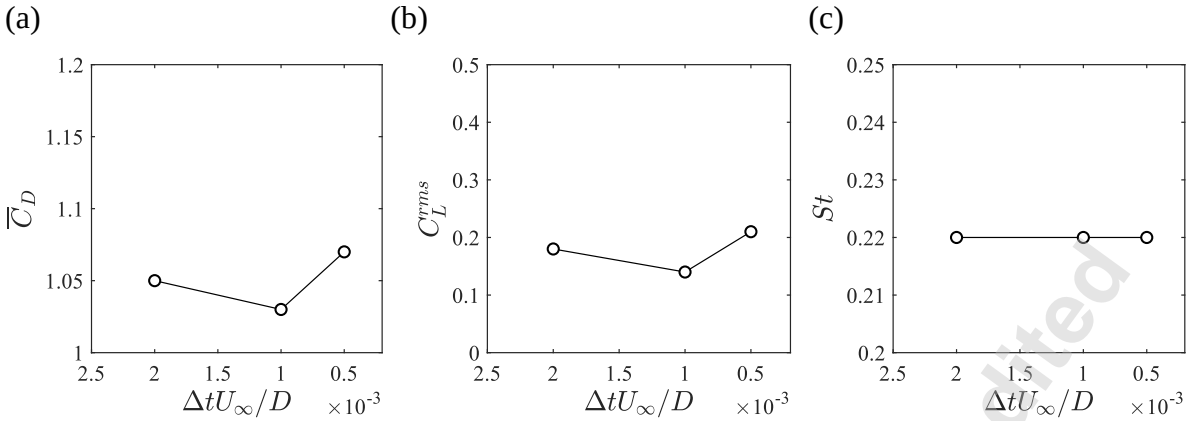

FIGURE 5: The temporal convergence study results: (a) $\overline{C_D}$; (b) C_L^{rms}; (c) St.

A series of simulations using the normal density mesh variant with 5031296 cells and time step of $\Delta tU_\infty/D = 0.002$ is performed and the results are compared with the previously published experimental measurements under the same flow conditions to validate the present numerical model. Fig. 6 (a) shows the comparison of the time- and spanwise-averaged streamwise velocity component (U_x/U_∞) in the wake of the cylinder (centerline in the *x*-*y* plane) from the present simulation with the experimental data from Parnaudeau et al. [19], Ong and Wallace [20] and Lourenco and Shih [21]. There is a good agreement between the present values of U_x/U_∞ and measurements made by Parnaudeau et al. [19]. A more detailed validation study in terms of the power spectral densities of the fluctuating components of the cross-flow velocity at different locations in the wake of the cylinder, the time-averaged velocity profiles and the Reynolds stress profiles can be found in Janocha et al. [18]. Based on these results, it can be concluded that the simulations results are in a very good agreement with the experimental data. The present numerical model appears to be suitable for investigating fluid-structure interaction problems of bluff bodies at $Re = 3900$.

Journal of Offshore Mechanics and Arctic Engineering. Received March 04, 2022;
Accepted manuscript posted June 27, 2022. doi:10.1115/1.4055281

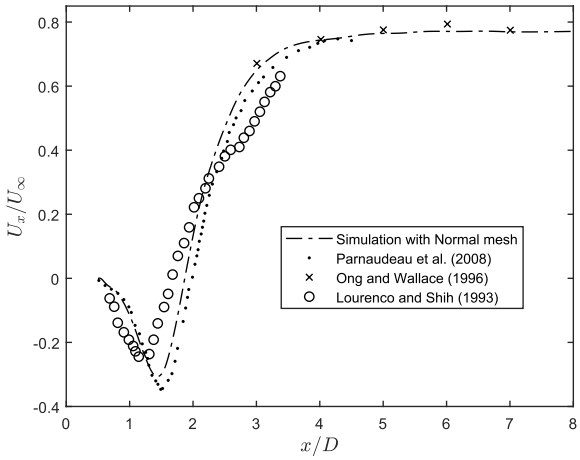

FIGURE 6: The comparison of the time- and spanwise-averaged streamwise velocity component (U_x/U_∞) in the wake of the cylinder (centerline in the *x*-*y* plane) with experimental data from Parnaudeau et al. [19], Ong and Wallace [20] and Lourenco and Shih (data taken from Beaudan and Moin [21]).

3.3 Simulations results of Self-excited Cylinder Vibrations

A series of numerical simulations of a cylinder undergoing vortex-induced vibration is performed and discussed in this section. The physical properties of the modeled cylinder are set to be $m^* = 2.6$ and $Re = 3900$, to approximate the experimental setup used by Assi et al. [22] ($m^* = 2.6$, $Re \in [3300, 5833]$). Three simulation cases are performed for $Ur \in [4, 5, 7]$. For each simulation, the first 10 oscillation cycles are removed from the analysis to exclude the effect of initial transient and the fully developed flow state is considered. An example of the fully developed flow state can be seen from the time-series of the cross-flow displacement and C_L at $Ur = 5$ in Fig 7. Figure 8 shows the normalized cross-flow displacement $\hat{y}/D$ predicted by the present simulations compared with the experiment conducted by Assi et al. [22]. In the upper branch of the VIV response with $Ur = 4$ and $Ur = 5$ shown in Fig. 8 the results from the simulation cases are slightly lower than the experimental results possibly due to the different Re values. For the experiment at $Ur = 4$, $Re = 3300$, at $Ur = 5$, $Re = 4166$ and at $Ur = 7$, $Re = 5833$ while in the simulations a constant $Re = 3900$ is used.

Journal of Offshore Mechanics and Arctic Engineering. Received March 04, 2022;
Accepted manuscript posted June 27, 2022. doi:10.1115/1.4055281

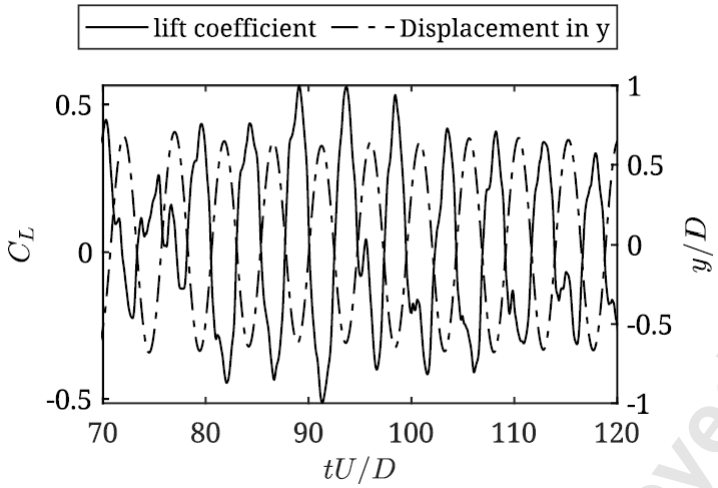

FIGURE 7: Time series of the lift coefficient and the cross-flow displacement for $Ur = 5$.

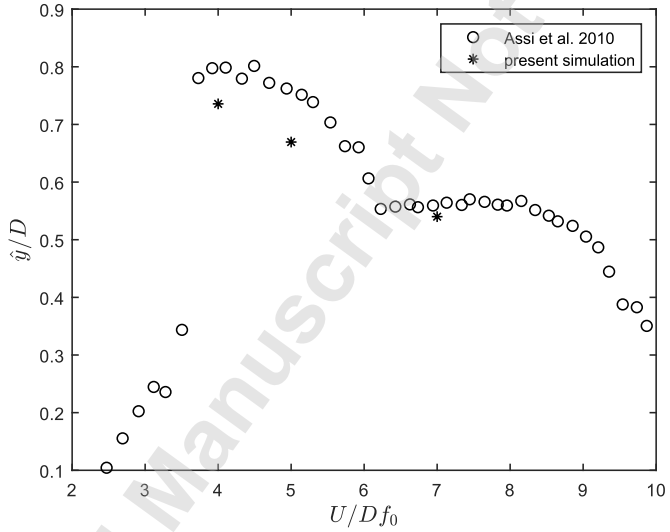

FIGURE 8: The comparison of normalized cross-flow vibration amplitudes obtained by the present simulations compared with experimental measurements by Assi et al. [22].

Power spectral densities of the lift and drag coefficients C_l and C_d of the vibrating cylinder are computed to identify the dominant frequencies of hydrodynamic forces. The spectral values are normalized by their max value. Fig. 9 show the power spectral densities of C_l and C_d for the investigated simulation cases. For the case with $Ur = 4$ shown in Fig. 9 (a), the dominant peak in the $|\hat{C}_L|$ spectra occur at $f/f_n = 0.84$ and the dominant peak in the spectra of $|\hat{C}_D|$ occurs at $f/f_n = 1.67$. The power spectra of $|\hat{C}_L|$ for the case with $Ur = 5$ shown in Fig. 9 (b) display a clear peak around $f/f_n = 3.1$ which indicates presence of a third harmonic component in the lift force. For the case with $Ur = 7$ as shown in Fig. 9 (c), there is a secondary peak at $f/f_n = 2.5$ close to the dominant peak at $f/f_n = 2.2$ for the drag force. This can explain the beating of the drag force since the interference between two signals with slightly

Journal of Offshore Mechanics and Arctic Engineering. Received March 04, 2022;
Accepted manuscript posted June 27, 2022. doi:10.1115/1.4055281

different frequencies will result in a periodic variation in signal amplitude with a frequency that is the difference of the two interfering frequencies. There is an also clear peak at $f/f_n = 0.3$ in the drag force spectra as a result of the beating phenomenon.

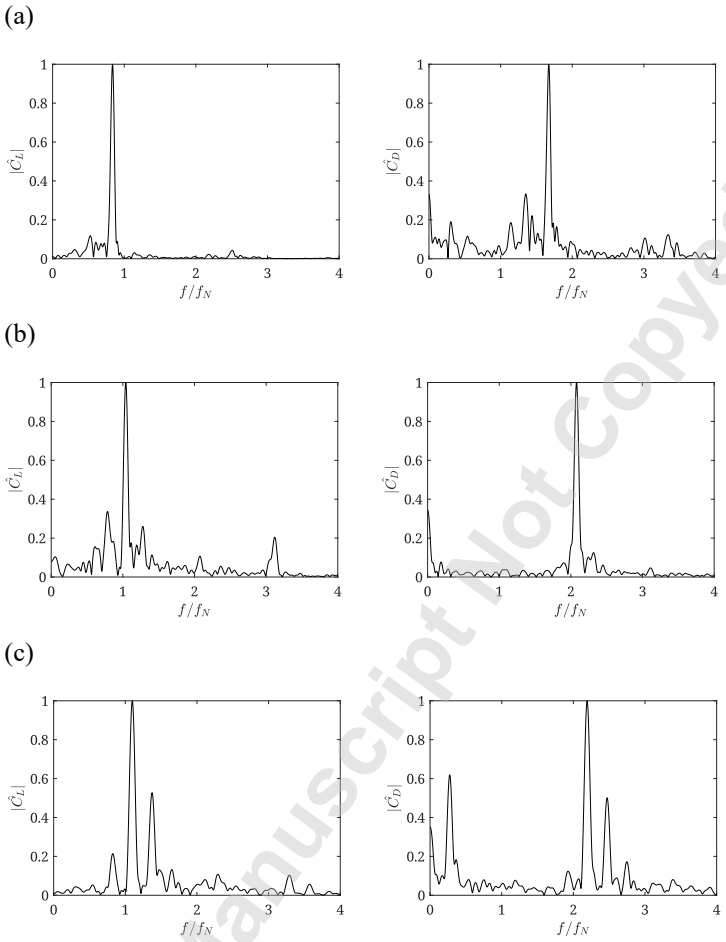

FIGURE 9: The normalized power spectral density of lift (left) and drag (right) coefficients for (a) $Ur = 4$; (b) $Ur = 5$; (c) $Ur = 7$.

For the identification of vortex shedding modes, the iso-surfaces of the pressure coefficient and the Q-criterion are shown in a three-dimensional (3D) view of Figs. 10~13. The iso-surfaces are colored by spanwise vorticity magnitude, where blue color indicates clockwise vortex rotation and red color indicates counterclockwise rotation. The 3D view of Cp iso-surface shown in Fig. 10 clearly reveals the 2S shedding pattern, where a single clockwise and a single counterclockwise vortex are shed. All vortices on one side rotate in the same direction and the rotation direction changes with each vortex that is shed per cycle. The turbulent wake structures for the simulation case with $Ur = 5$ are shown in Figs. 11 (a) and (b). The vortex shedding mode is also clasified as 2S type. The Cp iso-surface pattern looks similar to that observed for the case with $Ur = 4$ shown in Fig. 10. Compared with the case with $Ur = 4$, the vortex cores in the case with $Ur = 5$ are more distorted with secondary longitudinal vortices developing in the

Journal of Offshore Mechanics and Arctic Engineering. Received March 04, 2022;
Accepted manuscript posted June 27, 2022. doi:10.1115/1.4055281

$x-y$ direction between the main spanwise vortices. During the buildup of the simulation when the cylinder starts to oscillate the vortex shedding mode changes temporarily to a $2P_o$ pattern. The $2P_o$ pattern defined by Morse and Williamson [23] is a pattern similar to 2P but the secondary vortex is much weaker. This shedding pattern occurs when the cross-flow displacement reaches the maximum value around $tU/D = 20$ and a corresponding snapshot of Cp iso-surface is shown in Fig. 12. Fig. 13 shows the wake structures for the simulation case with $Ur = 7$. For this simulation case, a 2P vortex shedding pattern is identified. The Q-criterion iso-surface colored by z-vorticity shows two closely spaced positive and negative vorticity zones that are shed every half-cycle of vibration, which represents two vortices rotating in opposite direction. It is also observed that the secondary vortex in each pair is weaker and smaller.

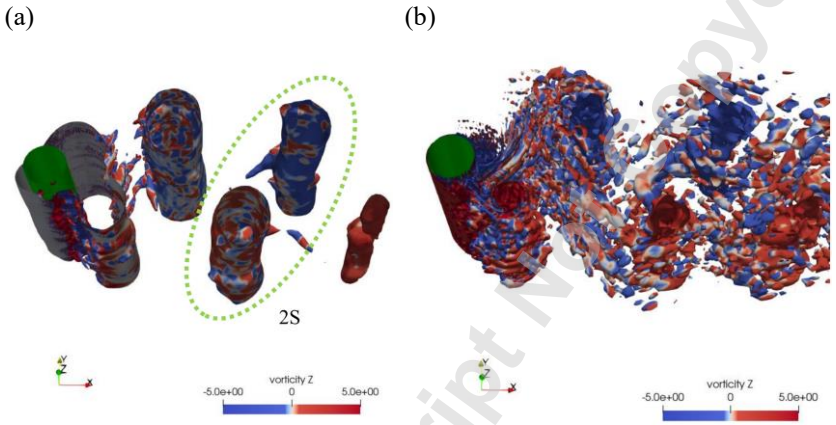

FIGURE 10: The iso-surface of (a) the pressure coefficient $(Cp = -0.25)$ and (b) the Q-criterion $(Q = 1)$colored by spanwise vorticity for $Ur = 4$ at $tU_\infty/D = 130$.

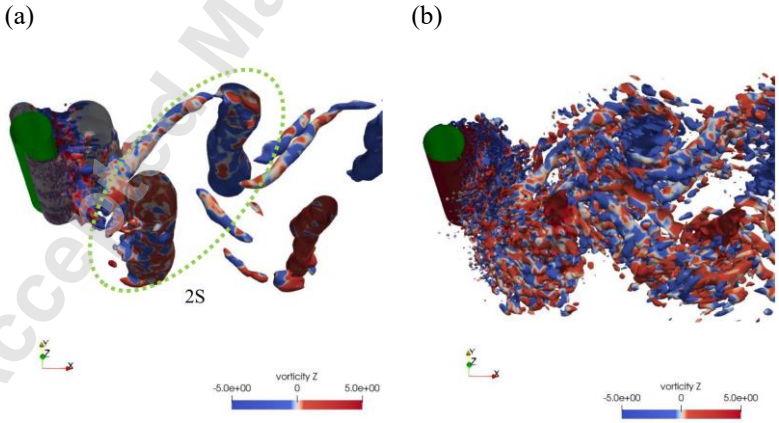

FIGURE 11: The iso-surface of (a) the pressure coefficient $(Cp = -0.25)$ and (b) the Q-criterion $(Q = 1)$colored by spanwise vorticity for $Ur = 5$ at $tU_\infty/D = 140$.

Journal of Offshore Mechanics and Arctic Engineering. Received March 04, 2022;
Accepted manuscript posted June 27, 2022. doi:10.1115/1.4055281

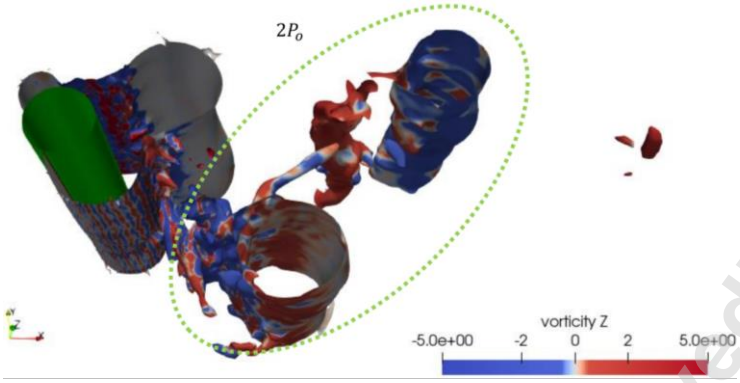

FIGURE 12: The iso-surface of pressure coefficient $(Cp = -0.2)$ colored by spanwise vorticity for $Ur = 5$ at $tU_\infty/D = 19.6$.

(a) (b)

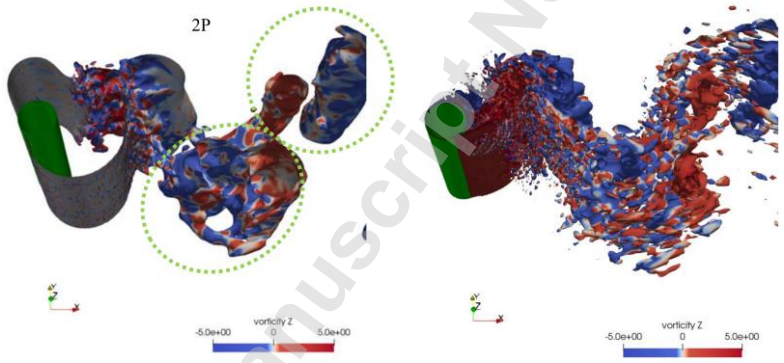

FIGURE 13: The iso-surface of (a) the pressure coefficient $(Cp = -0.1)$ and (b) the Q-criterion $(Q = 1)$colored by spanwise vorticity for $Ur = 7$ at $tU_\infty/D = 160$.

3.4 Proper Orthogonal Decomposition analysis

The Proper Orthogonal Decomposition (POD) first proposed by Lumley [24] is a technique that extracts the basis for a modal decomposition from an ensemble of a random vector field (Berkooz et al., [25]). In fluid mechanics POD is frequently employed to identify the dominant, energy containing, coherent structures in the flow. In POD analysis, any time-dependent variables $q(\chi, t)$ (where χ denotes the coordinates and t is the time) can be decomposed into different modes, $\phi_i(\chi)$, and their temporal coefficients $a_i(t)$ as $q(\chi, t) = \sum_i a_i(t)\,\phi_i(\chi)$. To extract these modes, the sampled data is arranged in the matrix M containing the cartesian components of a random vector field as:

$$M = [v_1, v_2, \ldots, v_n] \qquad (10)$$

Journal of Offshore Mechanics and Arctic Engineering. Received March 04, 2022;
Accepted manuscript posted June 27, 2022. doi:10.1115/1.4055281

Then, applying the Singular Value Decomposition (SVD) on the matrix M gives the POD modes as $M = U\Sigma V^T$ where V and U are, respectively, the right and left singular vectors of M, and Σ denotes the diagonal matrix. The matrix U contains the POD modes $\phi_j(\chi)$ in column vectors and the matrix V contains the temporal coefficients $a_j(t)$. Both U and V are orthogonal matrices as $U^TU = I$ and $V^TV = I$. The diagonal matrix Σ contains the singular values of the matrix M ($\Sigma = \text{diag}(\lambda_1, \lambda_2, \lambda_3 \ldots \lambda_n)$ where each diagonal value represents energy of each POD mode and are ranked as $\lambda_1 > \lambda_2 > \lambda_3 > \ldots > \lambda_n > 0$.

In the present study, the POD is performed on data vector containing the three orthogonal components of the velocity field. For the analyses of the turbulent wake of a vibrating cylinder the POD is carried out on data sampled from the cylinder's wake for three cases with different Ur. One plane normal to the spanwise direction and a set of 2D planes normal to the flow direction and are used to formulate the POD basis. Similar POD analysis is also reported in Serta Fraga et al. [26]. The location of sampling planes is shown in Fig. 14. The sampling interval is set to $\Delta t U_\infty/D = 0.02$ which corresponds to every 10th time step in the present CFD simulations. The uncertainty of the POD analysis can be quantified by assessing the convergence of POD modes. To achieve the mode convergence, enough snapshots of the flow field must be used in the mode decomposition and the sampling interval must be small enough. The basic assumption is that with increasing number of snapshots or with the sampling interval refinement, the most energetic modes spatial structures will converge towards the same solution. This method is based on the orthogonality between modes as proposed by Muld et al. [27] and also used in Serta Fraga et al. [26]. The orthogonality is a property of POD and for identical modes it is equal to 1. In the present study, the orthogonality is computed for the leading 10 modes as $\delta_{ortho} = \langle \boldsymbol{\phi}_{i,1}, \boldsymbol{\phi}_{i,2} \rangle$, where i=1…10 is the mode number, $\boldsymbol{\phi}_{i,1}$ are the leading POD spatial modes of the reference solution and $\boldsymbol{\phi}_{i,2}$ are the leading POD spatial modes of the compared solution. The results of the mean computed δ_{ortho} for different snapshot numbers and different sampling intervals are shown in Fig. 15. It can be seen that a convergence trend can be achieved with a number of snapshots larger than 600 and $\Delta t U_\infty/D$ smaller than 0.2. Therefore, the present adopted sampling intervals and number of snapshots can be regarded as appropriate.

Journal of Offshore Mechanics and Arctic Engineering. Received March 04, 2022;
Accepted manuscript posted June 27, 2022. doi:10.1115/1.4055281

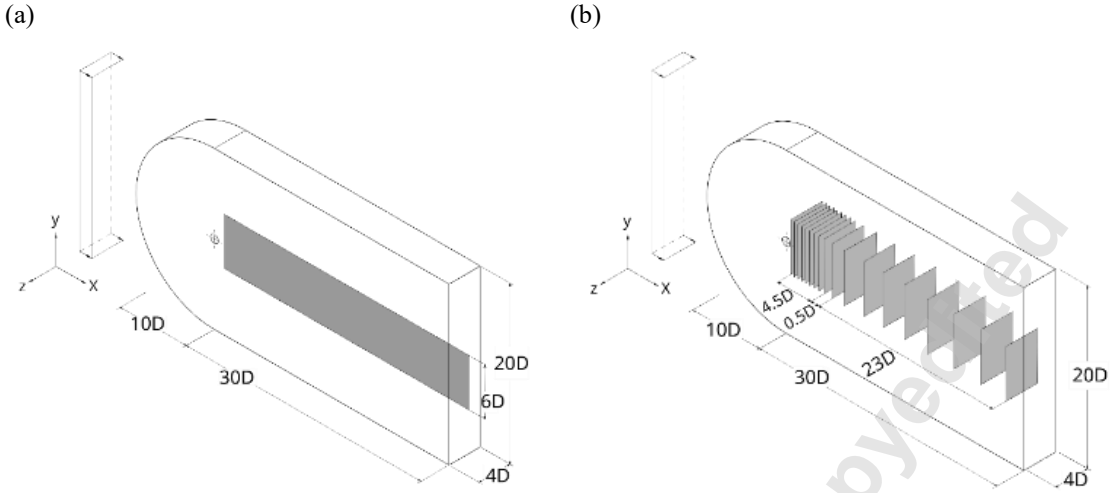

FIGURE 14: Schematic of the data sampling planes locations in the computational domain (a) XY plane; (b) XZ planes.

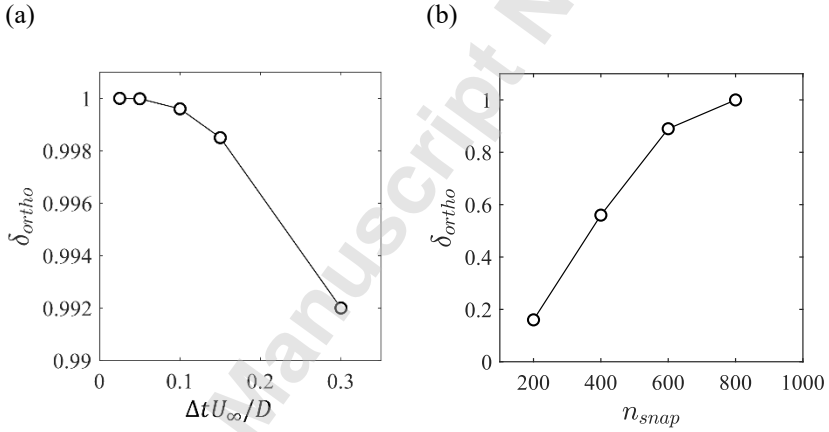

FIGURE 15: POD mode convergence: (a) sensitivity of the sampling time step (Δt_{snap}); (b) sensitivity of the number of data snapshots (n_{snap}). The mean value of δ_{ortho} of the ten dominant modes between different (a) sampling intervals; (b) numbers of snapshots.

3.4.1 POD mode distribution on the XY-plane

Modal decomposition of the turbulent wake for three different Ur is presented on the XY plane. Fig. 16 shows the fluctuating kinetic energy of each mode and cumulative fluctuating kinetic energy of all 800 POD modes for $Ur = 4, 5$ and 7. To capture 90% of the energy of the flow, the 114, 142 and 82 most energetic modes are required to reconstruct the flow fields for $Ur = 4, 5$ and 7, respectively. Fig. 17 presents the energy contribution of the leading 20 POD modes for each Ur. The POD modes come in pairs with similar energy. There is a large separation between

Journal of Offshore Mechanics and Arctic Engineering. Received March 04, 2022;
Accepted manuscript posted June 27, 2022. doi:10.1115/1.4055281

the energy of the first two leading modes and the higher order modes. Modes 1 and 2 (denoted also as ϕ_1 and ϕ_2) have the energy contribution ranging from 6.6% to 9% while the higher modes contribute 4% or less to the total energy. It can be also seen that a large number of modes is required to accurately reconstruct the flow field. However, the main flow features can be revealed by only a few leading modes.

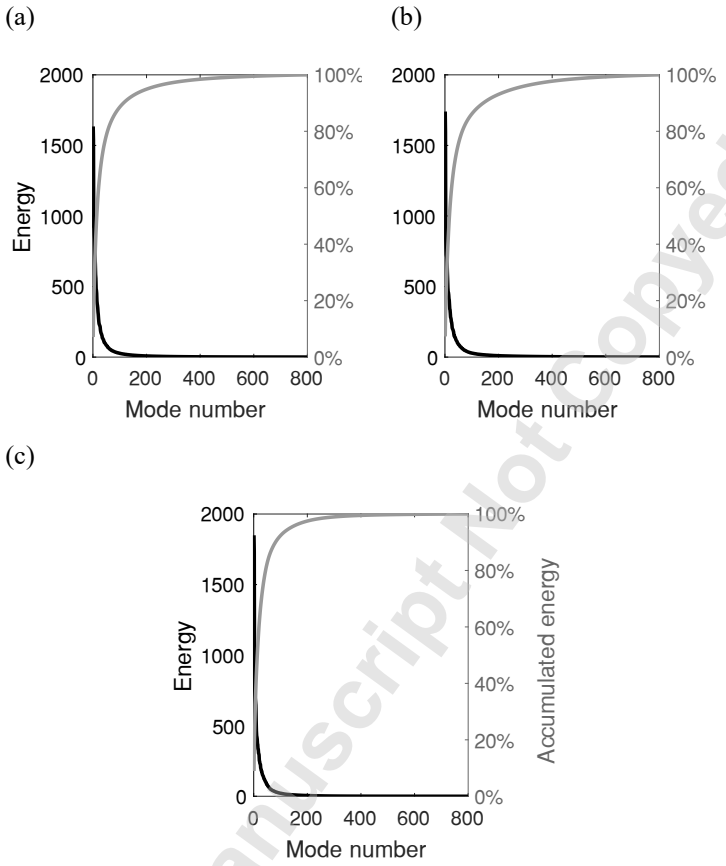

FIGURE 16: Energy and accumulated energy of POD modes on the XY plane; (a) $Ur = 4$; (b) $Ur = 5$; (c) $Ur = 7$.

Journal of Offshore Mechanics and Arctic Engineering. Received March 04, 2022;
Accepted manuscript posted June 27, 2022. doi:10.1115/1.4055281

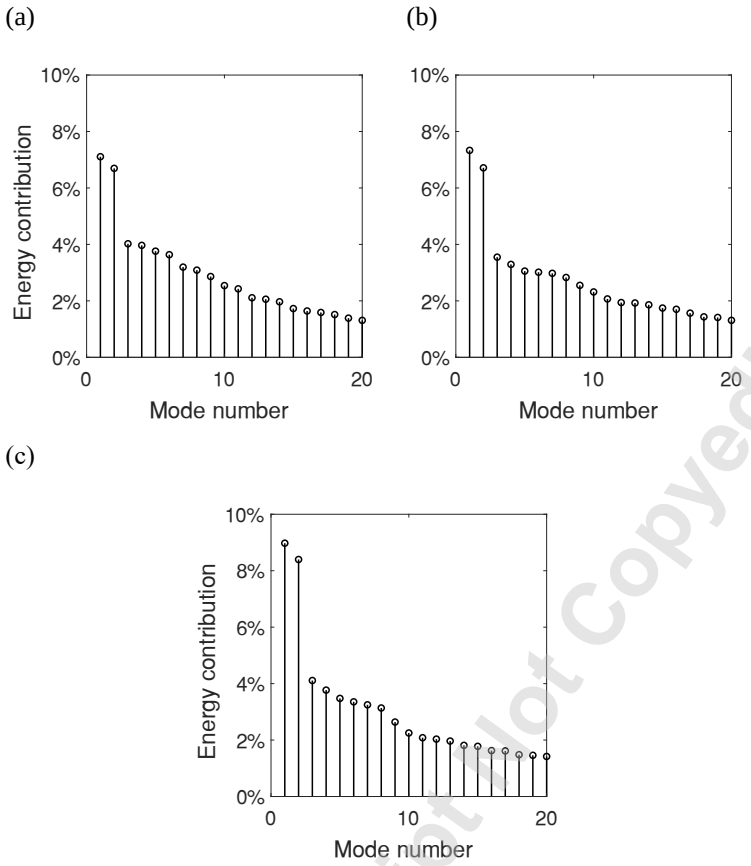

FIGURE 17: The Energy contribution of the first 20 POD modes on the XY plane; (a) $Ur = 4$; (b) $Ur = 5$; (c) $Ur = 7$.

The time coefficients a_i and their power spectral density (PSD) of the first two leading modes are shown in the Figs. 20~22 for $Ur = 4, 5$ and 7, respectively. The frequency of time coefficients for the first two leading modes is coincident with the Strouhal frequency for all investigated Ur, which indicates that the two leading modes may be associated with the energy containing primary vortex street. The time coefficients amplitudes of the first two leading modes are similar with a temporal shift, which indicates a traveling-wave behavior of the primary shedding vortices. The mode shapes of the two leading POD modes for all investigated Ur are shown in Fig. 18. The mode shapes of the u component for ϕ_1 and ϕ_2 is antisymmetric about the x-axis and can be associated with periodically shed vortices both in the upper and lower part of the wake flow. This is also a unique feature of the wake flow behind a vibrating cylinder, compared with the wake flow behind a stationary cylinder. The structure of the v component for ϕ_1 and ϕ_2 is symmetric about the x-axis and represents the transverse movement of the fluid in the cylinder's wake driven by the alternating vortex street. Due to the similarity both in the mode shapes and their temporal behavior, ϕ_1 and ϕ_2 can be named as a mode pair.

Journal of Offshore Mechanics and Arctic Engineering. Received March 04, 2022;
Accepted manuscript posted June 27, 2022. doi:10.1115/1.4055281

Similar mode pairs can be found among the higher order modes. The second harmonic mode pairs are presented in Fig. 19. Due to the frequency mixture of the POD modes as reported in Schmid [28], the second harmonic mode appears for different mode numbers for each investigated Ur. For $Ur = 4$, the pair of second harmonic modes are ϕ_7 and ϕ_8. They have a slightly lower energy contribution than $\phi_3 \sim \phi_6$ which display a chaotic flow structure and not presented here. The u component shown in Fig. 19 also displays an antisymmetric behavior with respect to x-axis and there is a quarter wavelength phase shift in the time coefficient which can be seen in Fig. 20 (b). This also indicates a travelling-wave characteristic. It is similar to the behavior of the first harmonic mode pair. The v component of the shapes displays clearly two traveling waves in the upper and lower part of the wake region and they display antisymmetric behavior with respect to x-axis. The mode shapes show smaller length scale compared with the first harmonic mode pair. For $Ur = 5$ as shown Fig. 21 (b), the second harmonic mode pair appears on ϕ_5 and ϕ_6. Compared with the second harmonic mode pair of $Ur = 4$, a chaotic behavior can be observed for that of $Ur = 5$, which is also observed in the mode shapes shown in Figs. 19 (c,d). The power spectra of the second harmonic mode pair shows a secondary frequency peak at $0.5f/St$ which can explain a less clear pattern compared to the case at $Ur = 4$. The second harmonic for $Ur = 7$ is represented by ϕ_3 and ϕ_4. They also show a secondary frequency peak at $0.5f/St$ in the power spectra densities of their time coefficients.

Journal of Offshore Mechanics and Arctic Engineering. Received March 04, 2022;
Accepted manuscript posted June 27, 2022. doi:10.1115/1.4055281

(a) POD Mode 1 at $Ur = 4$

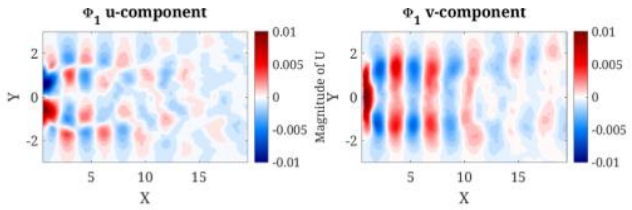

(b) POD Mode 2 at $Ur = 4$

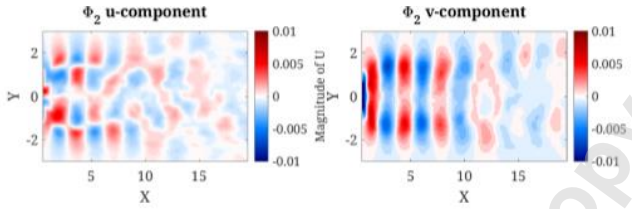

(c) POD Mode 1 at $Ur = 5$

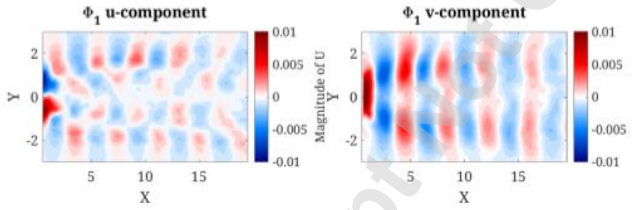

(d) POD Mode 2 at $Ur = 5$

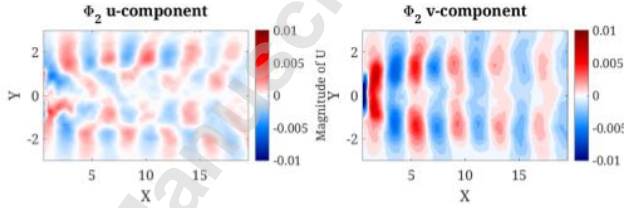

(e) POD Mode 1 at $Ur = 7$

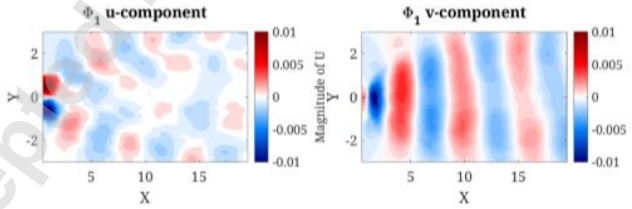

(f) POD Mode 2 at $Ur = 7$

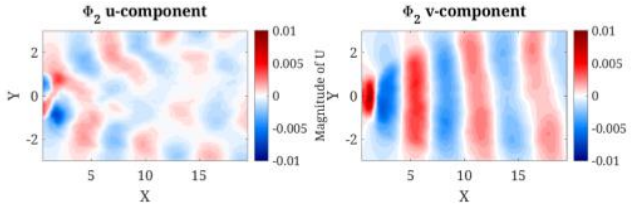

FIGURE 18: The mode shapes of two leading POD modes: (a, b) $Ur = 4$; (c, d) $Ur = 5$; (e, f) $Ur = 7$.

Journal of Offshore Mechanics and Arctic Engineering. Received March 04, 2022;
Accepted manuscript posted June 27, 2022. doi:10.1115/1.4055281

(a) POD Mode 7 at $Ur = 4$

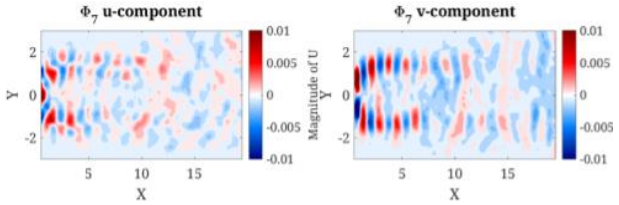

(b) POD Mode 8 at $Ur = 4$

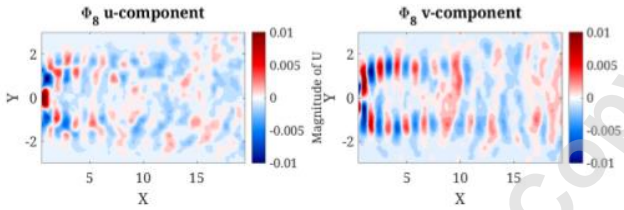

(c) POD Mode 5 at $Ur = 5$

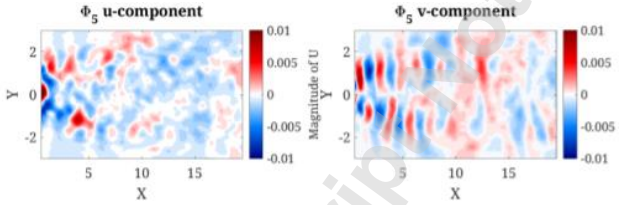

(d) POD Mode 6 at $Ur = 5$

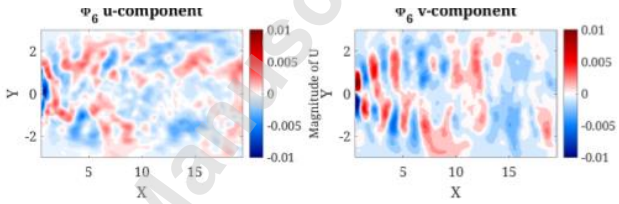

(e) POD Mode 3 at $Ur = 7$

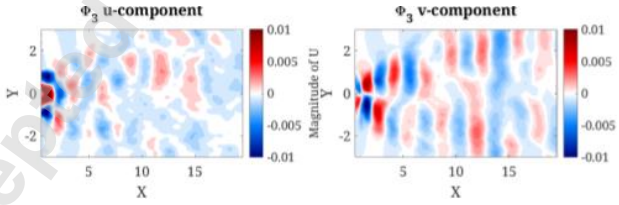

(f) POD Mode 4 at $Ur = 7$

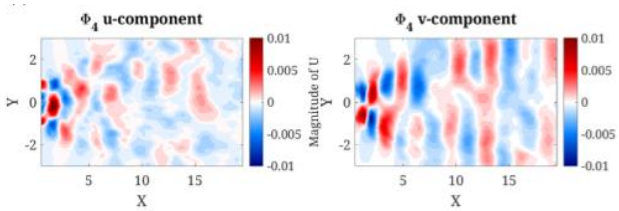

FIGURE 19: The second harmonic shedding POD modes: (a, b) $Ur = 4$; (c, d) $Ur = 5$; (e, f) $Ur = 7$.

Journal of Offshore Mechanics and Arctic Engineering. Received March 04, 2022;
Accepted manuscript posted June 27, 2022. doi:10.1115/1.4055281

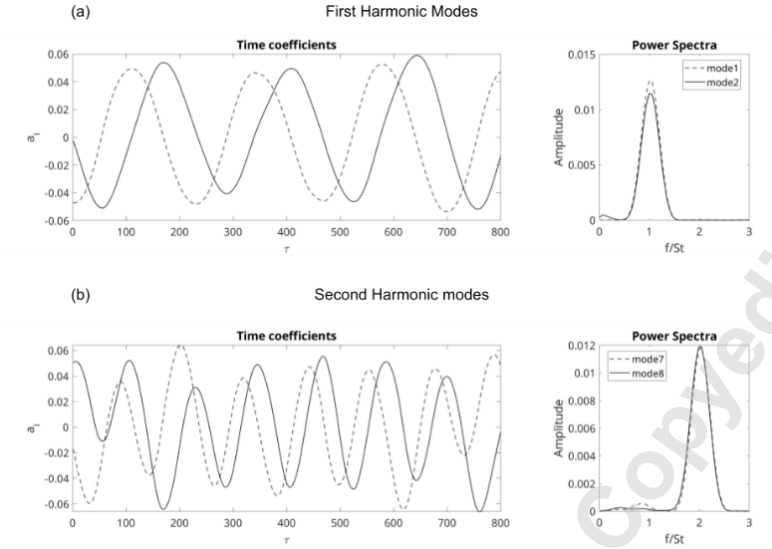

FIGURE 20: The time coefficients and power spectra for the harmonic mode pairs on the XY plane for $Ur = 4$: (a) the first harmonic mode pair; (b) the second harmonic mode pair.

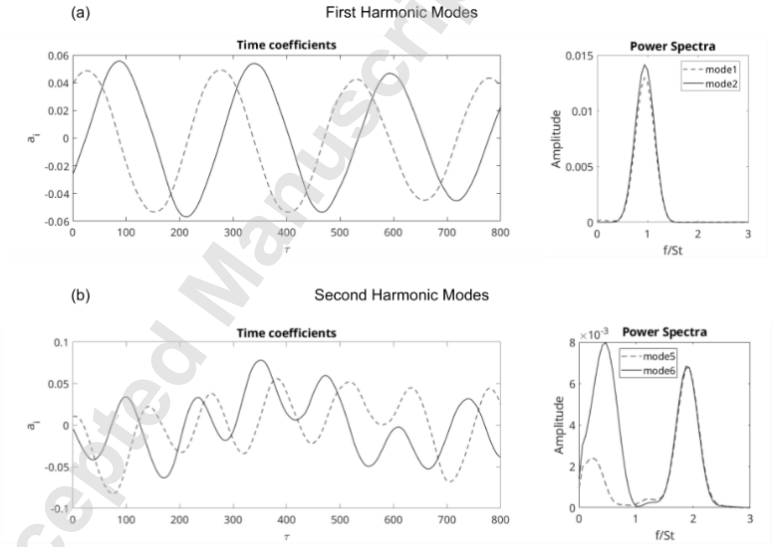

FIGURE 21: The time coefficients and power spectra for the harmonic mode pairs on the XY plane for $Ur = 5$: (a) the first harmonic mode pair; (b) the second harmonic mode pair.

Journal of Offshore Mechanics and Arctic Engineering. Received March 04, 2022;
Accepted manuscript posted June 27, 2022. doi:10.1115/1.4055281

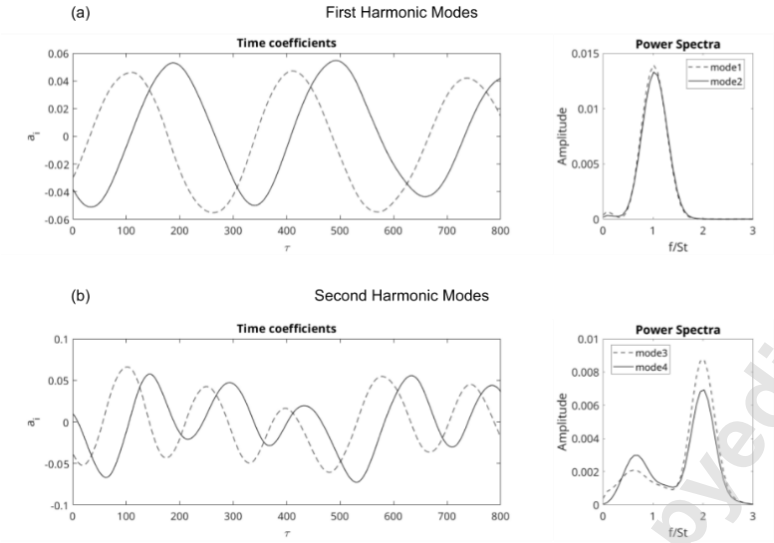

FIGURE 22: The time coefficients and power spectra for the harmonic mode pairs on the XY plane for $Ur = 7$: (a) the first harmonic mode pair; (b) the second harmonic mode pair.

To study the three-dimensional wake flow, the POD is further performed on multiple YZ planes normal to the flow direction in the wake region. The representative locations chosen for the analysis are located at distances of $x/D = 0.5, 1, 2, 4, 6, 8$ from the center of the cylinder.

The energy and accumulated energy for the POD modes is shown in the Figs. 23, 25, 27 and the energy contribution of the leading 20 modes is shown in Fig. 24, 26, 28. For the locations close to the cylinder, a larger number of POD modes is required to capture a sufficient percentage of the total amount of the energy, compared with the locations further downstream. With a distance of $x/D = 1$, the first 200 modes capture less than 85% of the energy as shown in Fig. 23 (b), while with the distance of $x/D = 6$, the first 200 modes capture close to 100% of the energy as shown in Fig. 23 (e). The first most energetic mode contributes between 7.4% and 12.6% of the total energy with different distances to the cylinder. The main difference between the distribution of the mode energy for the XY plane and the YZ planes is the lack of apparent mode pairing for the YZ planes. Compared to the cases for $Ur = 4$ and $Ur = 5$, it is noticeable that the energy contribution of the first most energetic mode is in general higher for $Ur = 7$ across all sampling locations as seen in Fig. 27. The difference in the energy contribution between the first most energetic mode and the second most energetic mode is also more significant for $Ur = 7$. The first mode has a energy contribution of more than 2 times the contribution of the second mode.

Journal of Offshore Mechanics and Arctic Engineering. Received March 04, 2022;
Accepted manuscript posted June 27, 2022. doi:10.1115/1.4055281

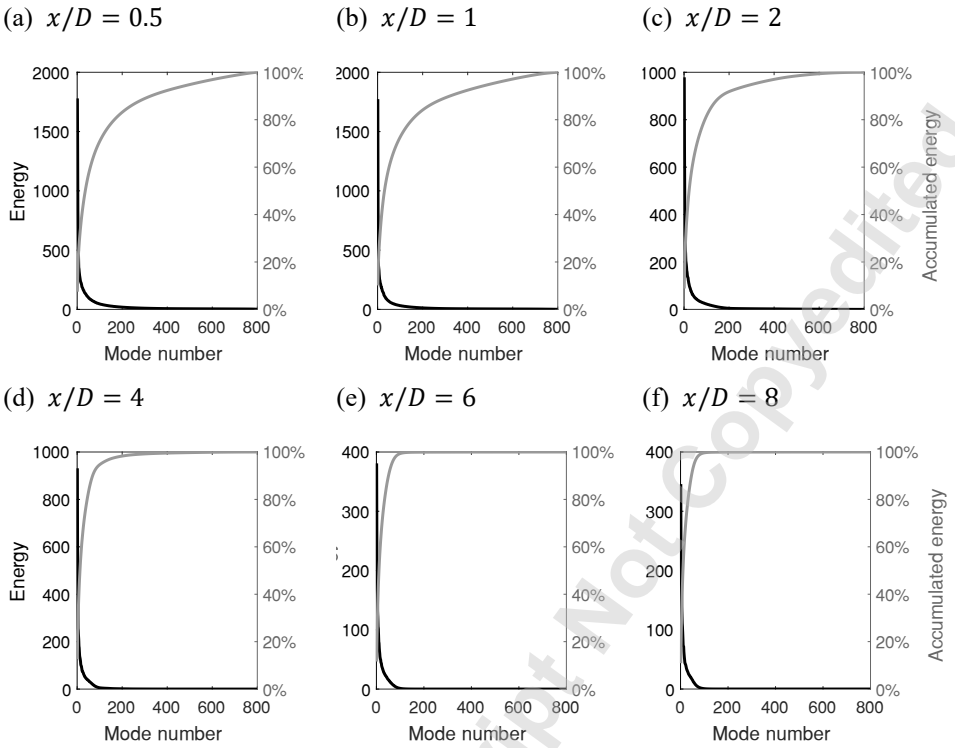

FIGURE 23: Energy and accumulated energy of POD modes for $Ur = 4$ on the YZ planes: (a) $x/D = 0.5$; (b) $x/D = 1$; (c) $x/D = 2$; (d) $x/D = 4$; (e) $x/D = 6$; (f) $x/D = 8$.

Journal of Offshore Mechanics and Arctic Engineering. Received March 04, 2022;
Accepted manuscript posted June 27, 2022. doi:10.1115/1.4055281

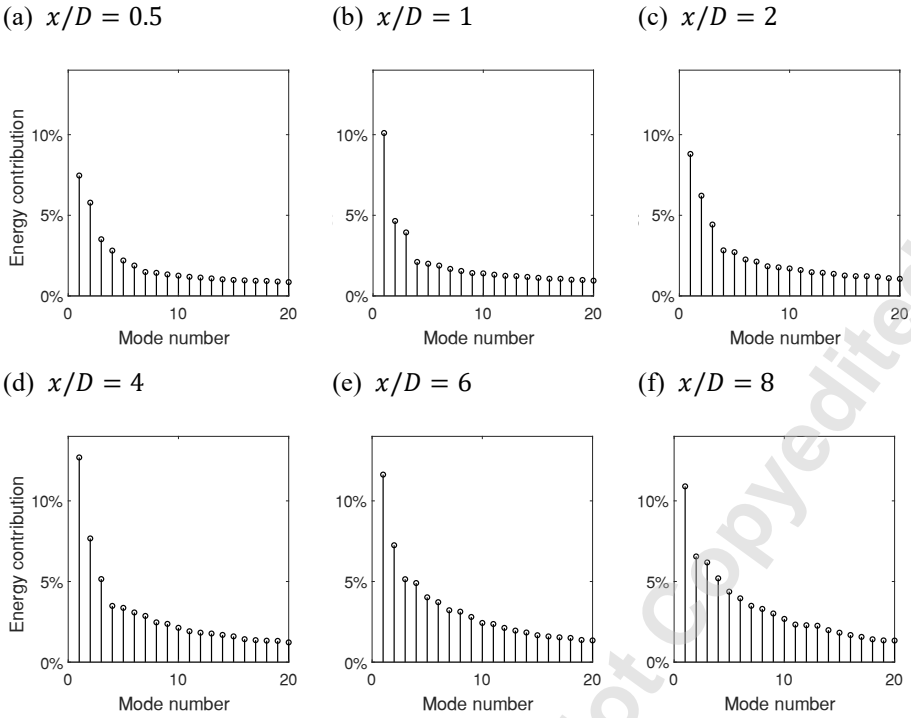

FIGURE 24: Energy contribution of the first 20 POD modes for $Ur = 4$ on the YZ planes: (a) $x/D = 0.5$; (b) $x/D = 1$; (c) $x/D = 2$; (d) $x/D = 4$; (e) $x/D = 6$; (f) $x/D = 8$.

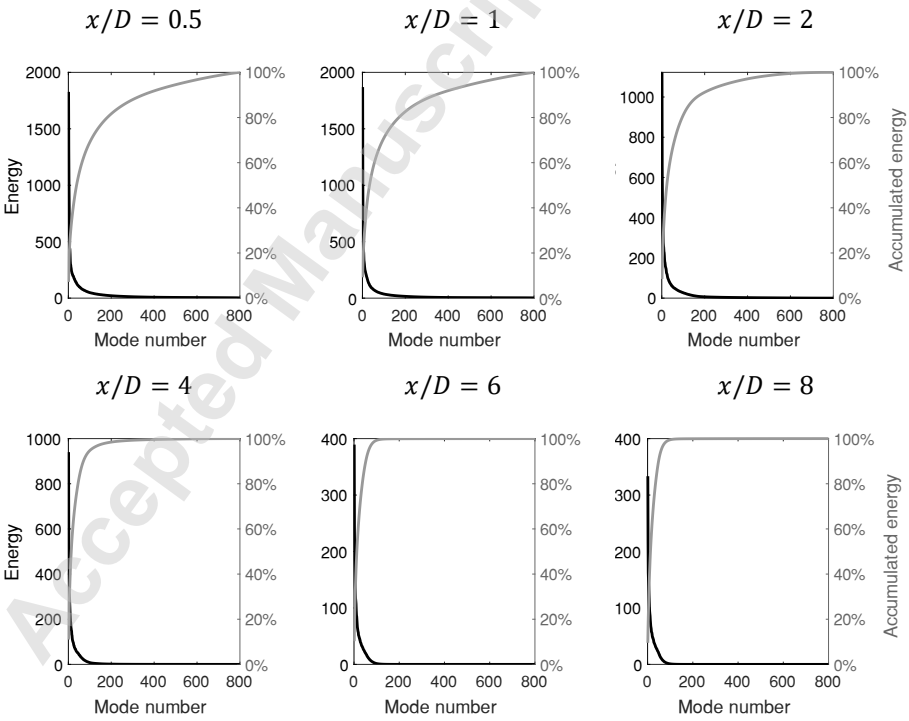

FIGURE 25: Energy and accumulated energy of POD modes for $Ur = 5$ on the YZ planes: (a) $x/D = 0.5$; (b) $x/D = 1$; (c) $x/D = 2$; (d) $x/D = 4$; (e) $x/D = 6$; (f) $x/D = 8$.

Journal of Offshore Mechanics and Arctic Engineering. Received March 04, 2022;
Accepted manuscript posted June 27, 2022. doi:10.1115/1.4055281

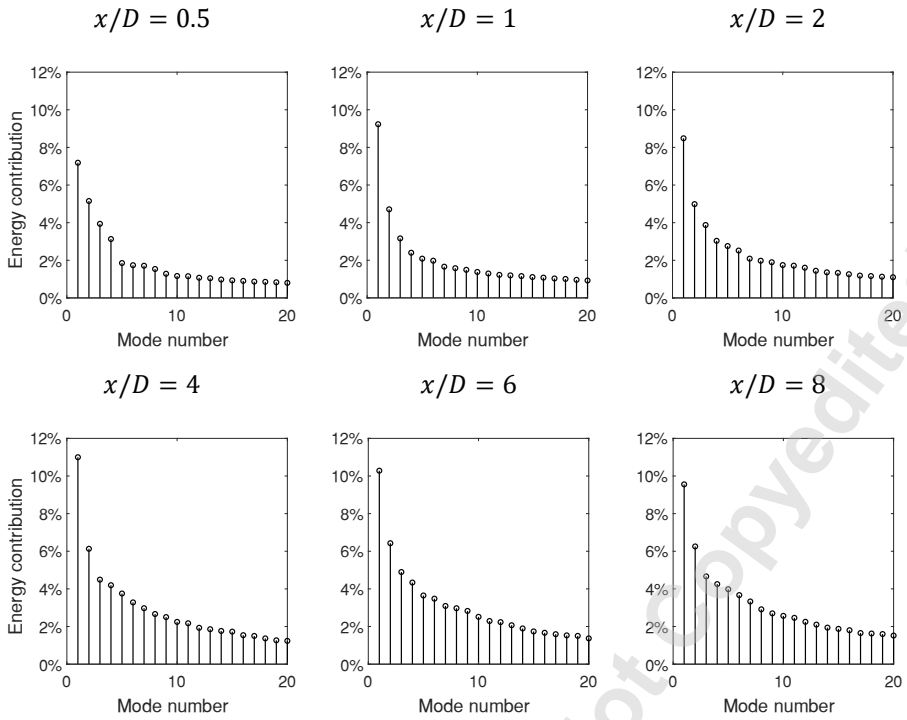

FIGURE 26: Energy contribution of the first 20 POD modes for $Ur = 5$ on the YZ planes: (a) $x/D = 0.5$; (b) $x/D = 1$; (c) $x/D = 2$; (d) $x/D = 4$; (e) $x/D = 6$; (f) $x/D = 8$.

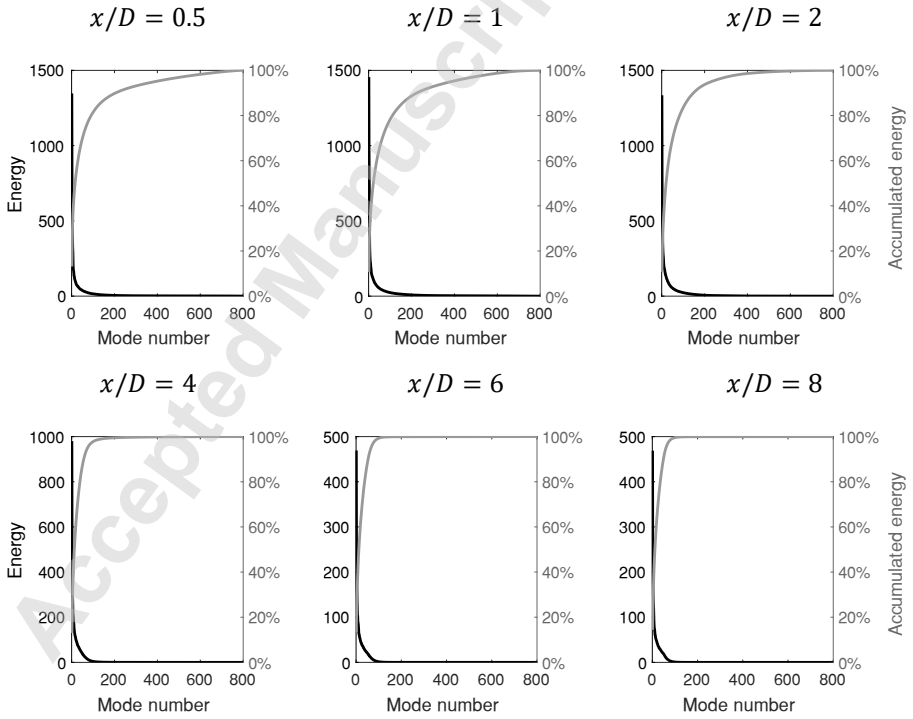

FIGURE 27: Energy and accumulated energy of POD modes for $Ur = 7$ on the YZ planes: (a) $x/D = 0.5$; (b) $x/D = 1$; (c) $x/D = 2$; (d) $x/D = 4$; (e) $x/D = 6$; (f) $x/D = 8$.

Journal of Offshore Mechanics and Arctic Engineering. Received March 04, 2022;
Accepted manuscript posted June 27, 2022. doi:10.1115/1.4055281

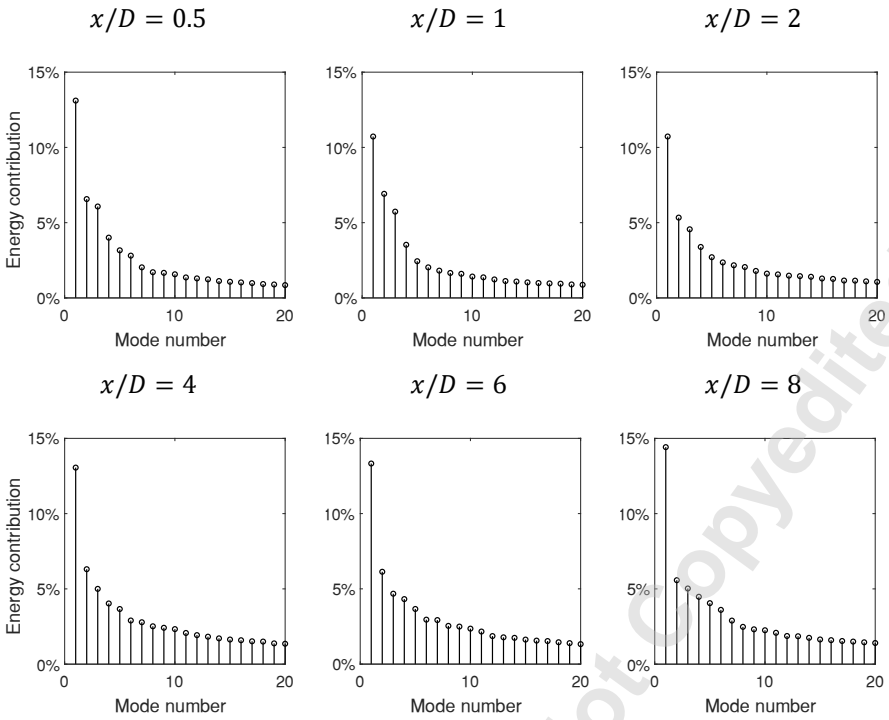

FIGURE 28: Energy contribution of the first 20 POD modes for $Ur = 7$ on the YZ planes: (a) $x/D = 0.5$; (b) $x/D = 1$; (c) $x/D = 2$; (d) $x/D = 4$; (e) $x/D = 6$; (f) $x/D = 8$.

Fig. 29 shows the spatial distribution of the v component for the Modes 1 to 4. For the first harmonic mode, the v component is symmetric around the centerline. For the second mode, the v component is antisymmetric around the centerline. Fig. 30 shows the spatial distribution of the w component for the Modes 1 to 4, which display strong three-dimensionality. For the w component of Mode 1 shown in Fig 30. (a), it can be seen that at a location close to the cylinder ($x/D \approx 0.5\sim1.5$), there are approximate two pairs of flow structures (as marked) which resemble vortex shedding cells. With the increasing streamwise location, their sizes are becoming larger. In addition, with the increasing mode order, the characteristic length scales of the flow structures are becoming smaller. Fig 31 shows the spatial distribution of the v component for Modes 1 to 4 with $Ur = 5$. Clear near-wake shear layer structures remain up to $x/D\sim2$. Compared with those for $Ur = 4$, pairs of more irregular and larger-scale flow structures cells can be observed in the w component of up to the 4th mode as shown in Fig 32. For $Ur = 7$, the v component of Modes 1 to 4 in Fig 33 shows only positive and negative spanwise uniform patches in each YZ plane up to $x/D\sim4$. For the w component in Fig 34, in the near-wake region, there are weak small-scale flow structures. Compared with those for $Ur = 4$ and 5, the cross-section spans of energetic motions tend to be smaller for $Ur = 7$. The spatial length scales of the flow structures in the downstream regions also tend to be smaller and more irregular compared with those for $Ur = 4$ and 5.

Journal of Offshore Mechanics and Arctic Engineering. Received March 04, 2022;
Accepted manuscript posted June 27, 2022. doi:10.1115/1.4055281

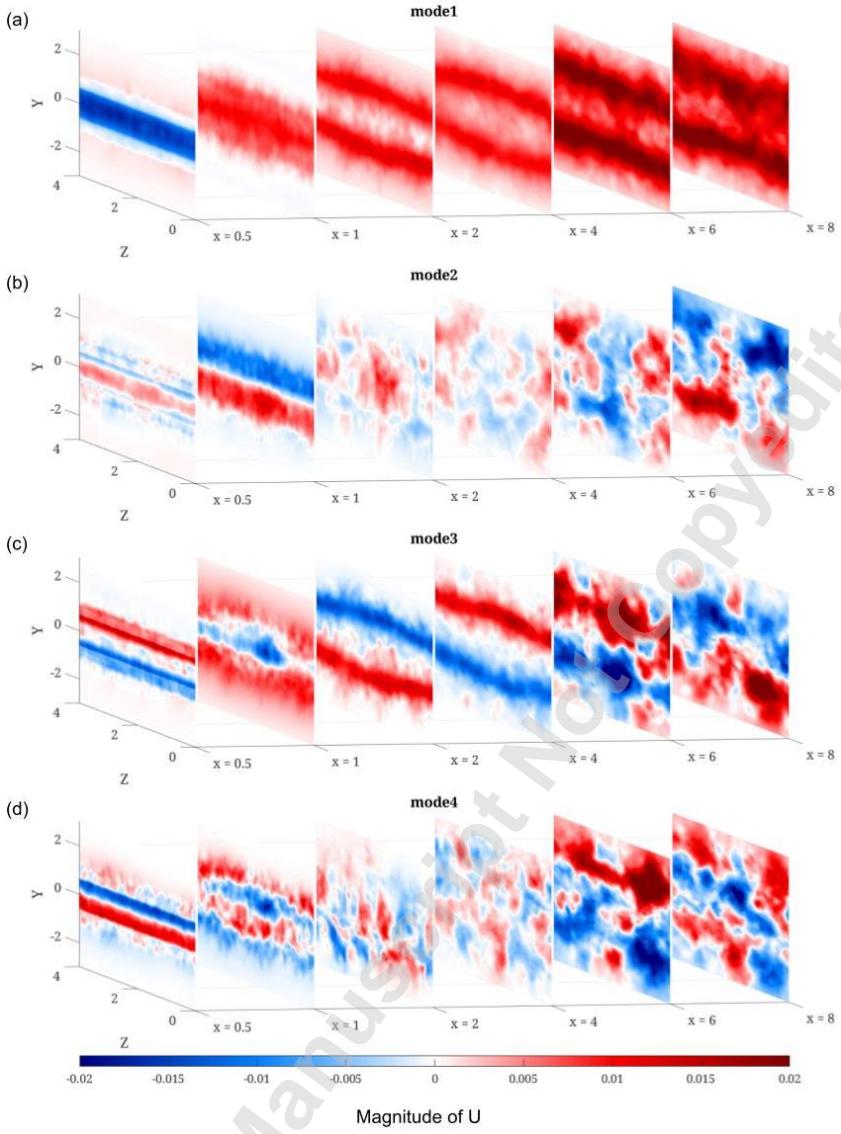

FIGURE 29: The v component of the POD modes at different x locations for $Ur = 4$: (a) Mode 1; (b) Mode 2; (c) Mode 3; (d) Mode 4.

Journal of Offshore Mechanics and Arctic Engineering. Received March 04, 2022;
Accepted manuscript posted June 27, 2022. doi:10.1115/1.4055281

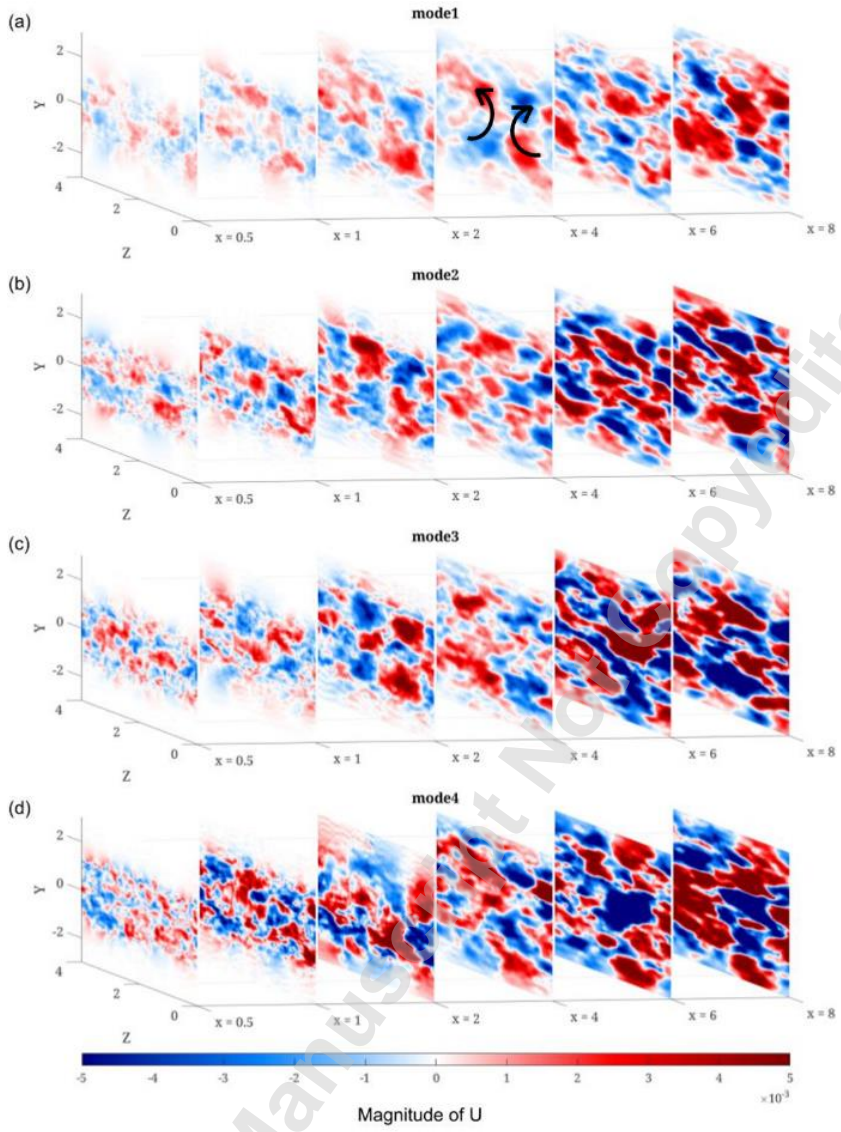

FIGURE 30: The w component of the POD modes at different x locations for $Ur = 4$: (a) Mode 1; (b) Mode 2; (c) Mode 3; (d) Mode 4.

Journal of Offshore Mechanics and Arctic Engineering. Received March 04, 2022;
Accepted manuscript posted June 27, 2022. doi:10.1115/1.4055281

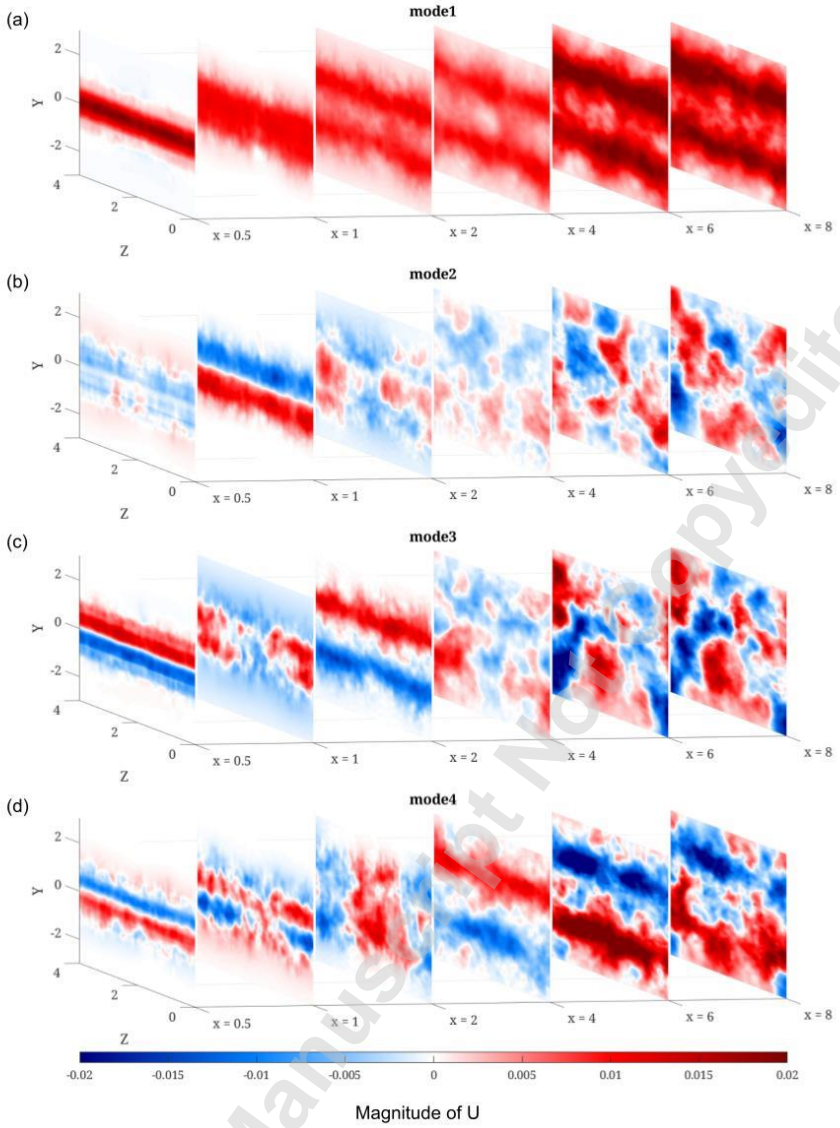

FIGURE 31: The v component of the POD modes at different x locations for $Ur = 5$: (a) Mode 1; (b) Mode 2; (c) Mode 3; (d) Mode 4.

Journal of Offshore Mechanics and Arctic Engineering. Received March 04, 2022;
Accepted manuscript posted June 27, 2022. doi:10.1115/1.4055281

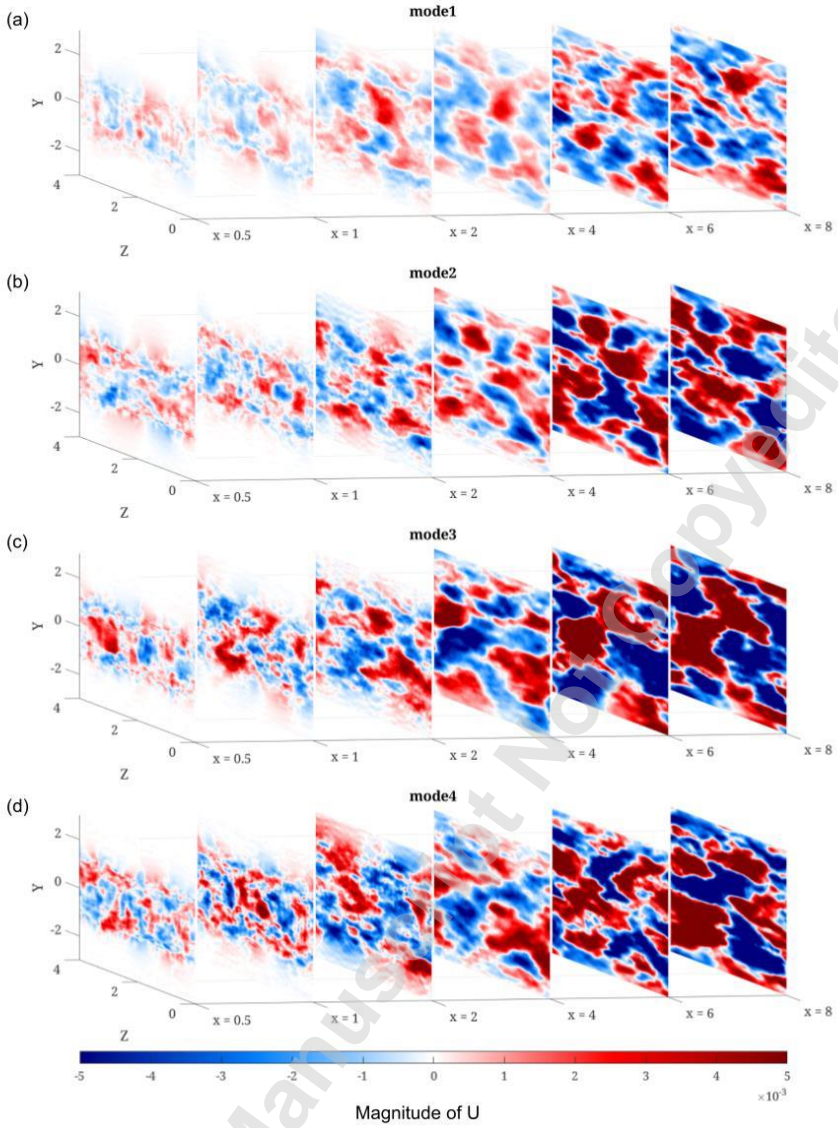

FIGURE 32: The w component of the POD modes at different x locations for $Ur = 5$: (a) Mode 1; (b) Mode 2; (c) Mode 3; (d) Mode 4.

Journal of Offshore Mechanics and Arctic Engineering. Received March 04, 2022;
Accepted manuscript posted June 27, 2022. doi:10.1115/1.4055281

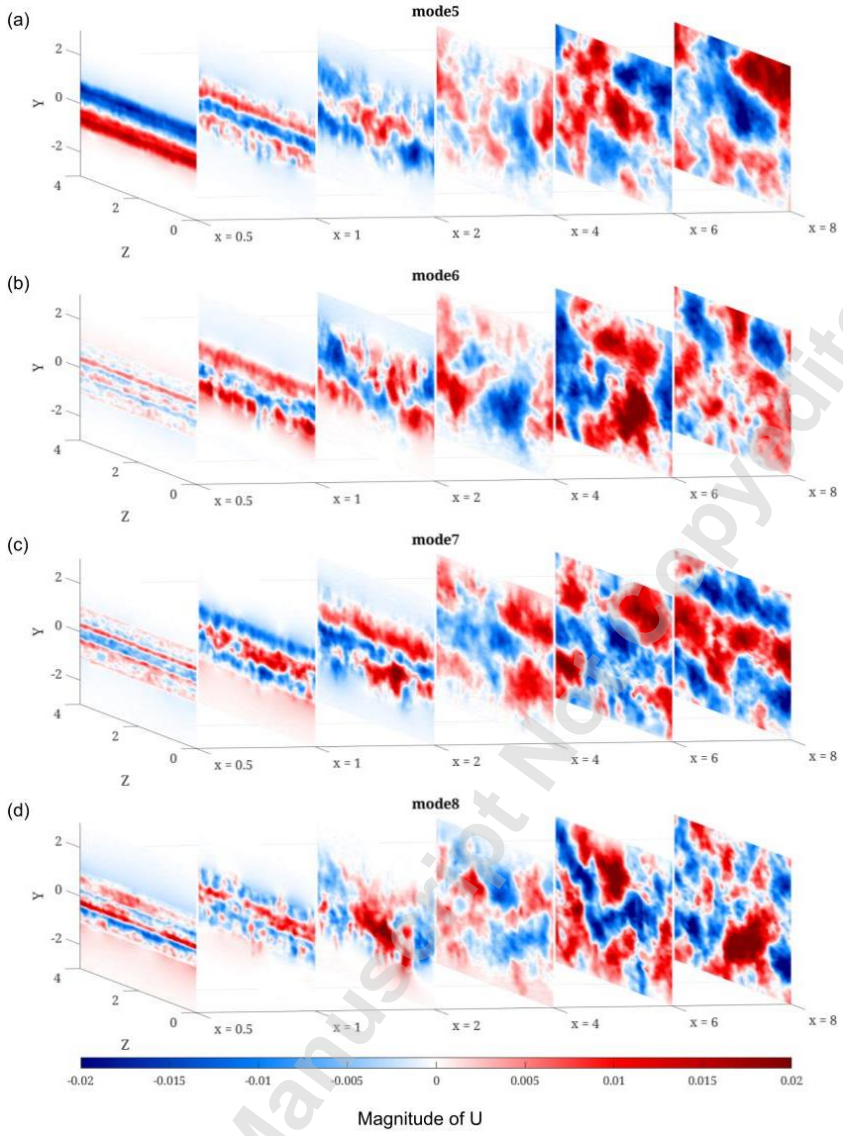

FIGURE 33: The v component of the POD modes at different x locations for $Ur = 7$: (a) Mode 1; (b) Mode 2; (c) Mode 3; (d) Mode 4.

Journal of Offshore Mechanics and Arctic Engineering. Received March 04, 2022;
Accepted manuscript posted June 27, 2022. doi:10.1115/1.4055281

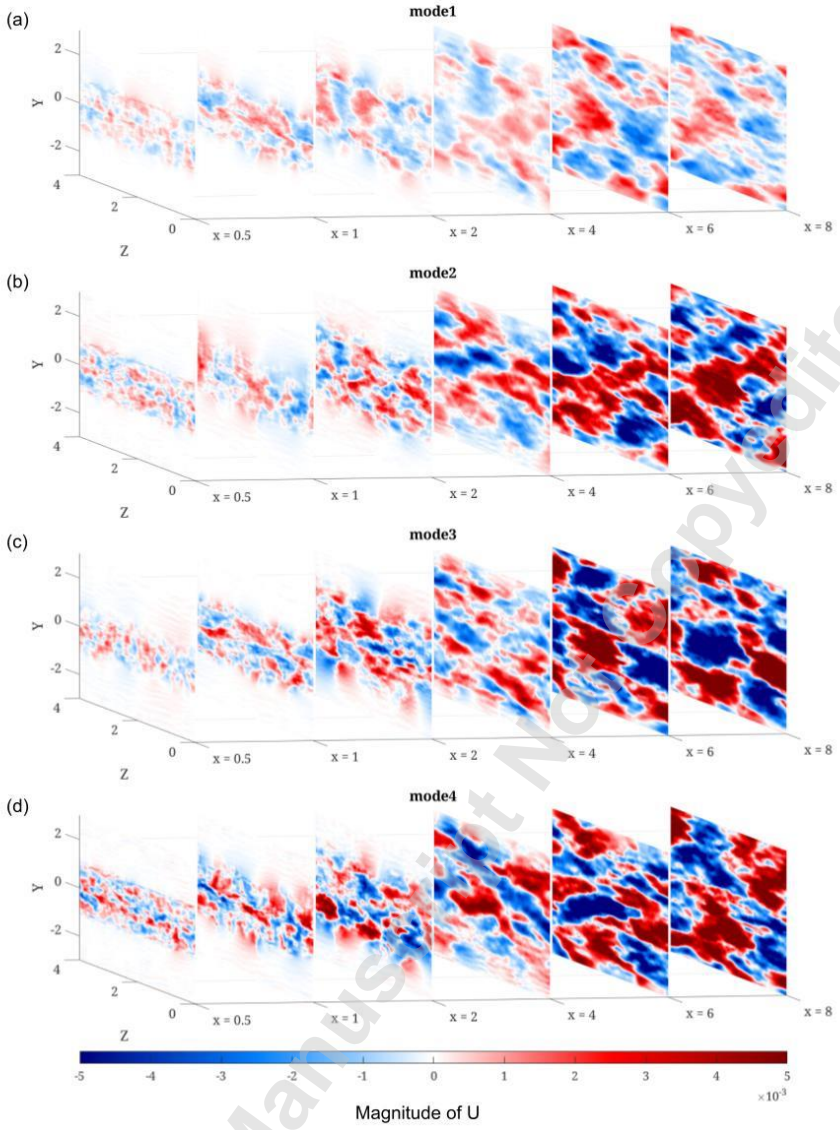

FIGURE 34: The w component of the POD modes at different x locations for $Ur = 7$: (a) Mode 1; (b) Mode 2; (c) Mode 3; (d) Mode 4.

4. Conclusion

In the present study, three-dimensional simulations of VIV are performed using Large Eddy Simulations (LES) and the wake flow structure is analyzed. The mesh and time-step convergence studies are performed for a stationary cylinder configuration. A mesh containing approximately 5×10^6 cells is found to achieve a good balance between the computational cost and the numerical accuracy. A time step of $\Delta tU_\infty/D = 0.002$ is found to give sufficient temporal resolution. The validation of the numerical model is performed by comparing the results obtained using the selected optimal mesh and time step with the previously published experimental data and numerical simulation results. The

predicted time- and spanwise-averaged flow velocities in the wake region, the pressure coefficient on the cylinder surface are found to be in good agreement with the experimental data and numerical simulation results.

Based on the simulation parameters of the stationary cylinder, the flow past an elastic mounted cylinder which is free to move in cross-flow direction is simulated. The simulation is performed at three different values of $Ur = 4, 5$ and 7. The lift and drag coefficients as well as the cross-flow displacement are obtained and analyzed. The displacements observed in the present simulations are slightly lower than experimentally measured displacements reported by Assi et al. [22]. Vortex shedding modes in the wake of the investigated cases are analyzed and classified by displaying the three-dimensional wake flow structures. The $2P_o$ mode is found during the initial phase in the simulation for $Ur = 5$. For further analyses of the wake flow structure, the POD analyses are performed on sampling planes in the wake to identify the coherent structure of the wake flow. The first and second harmonic mode pairs are found, and a traveling-wave behavior is observed in the wake. To study the three-dimensionality of the wake flow, the POD is performed on multiple YZ planes normal to the flow direction placed in representative locations in the wake region. The energy contribution of the dominant modes is increasing with an increasing Ur. Different from the spatial modes of the streamwise velocity component where the mode pairing is present, no apparent mode pairing is observed for the spatial modes of transverse and spanwise velocity components. Among the investigated Ur cases, the spatial patterns of the corresponding modes for the transverse and spanwise velocity components reveal that with increasing Ur, the spanwise length scales tend to become smaller.

Acknowledgements

This study was supported with computational resources provided by the Norwegian Metacenter for Computational Science (NOTUR) [Project No: NN9372K]

References

[1] Feng, C. C., 1968. "The measurement of vortex induced effects in flow past stationary and oscillating circular and D-section cylinders," Ph.D. thesis, University of British Columbia.

[2] Sumer, B. M., and Fredsøe, J., 2006. *Hydrodynamics around cylindrical structures*. World Scientific.

[3] Jauvtis, N. A., and Williamson, C. H. K., 2004. "The effect of two degrees of freedom on vortex-induced vibration at low mass and damping," *Journal of Fluid Mechanics*, **509**, pp.23-62.

[4] Assi, G. D. S., Meneghini, J. R., Aranha, J. A. P., Bearman, P. W. and Casaprima, E., 2006. "Experimental investigation of flow-induced vibration interference between two circular cylinders," *Journal of Fluids and Structures*, **22**(6-7), pp. 819-827.

[5] Govardhan, R. and Williamson, C. H. K., 2002. "Resonance forever: existence of a critical mass and an infinite regime of resonance in vortex-induced vibration," *Journal of Fluid Mechanics*, **473**, pp. 147-166.

[6] Griffith, M. D., Jacono, D. L., Sheridan, J., and Leontini, J. S., 2017. "Flow-induced vibration of two cylinders in tandem and staggered arrangements," *Journal of Fluid Mechanics*, **833**, pp. 98-130.

[7] Zhao, M., and Yan, G., 2013. "Numerical simulation of vortex-induced vibration of two circular cylinders of different diameters at low Reynolds number," *Physics of Fluids*, **25**(8), pp. 083601.

[8] Zhao, M., Midson, J., and Pearcey, T., 2016. "Vortex-induced vibration of side-by-side dual cylinders of different diameters," *Proc. The Twelfth ISOPE Pacific/Asia Offshore Mechanics Symposium. International Society of Offshore and Polar Engineers.* Gold Coast, Australia, pp. 193-198.

[9] Wu, W., Bernitsas, M. M., and Maki, K., 2014. "RANS simulation versus experiments of flow induced motion of circular cylinder with passive turbulence control at 35,000< Re< 130,000," *Journal of Offshore Mechanics and Arctic Engineering*, **136**(4), pp. 733-744.

[10] Janocha, M. J., and Ong, M. C., 2021. „Vortex-induced vibrations of piggyback pipelines near the horizontal plane wall in the upper transition regime," *Marine Structures*, **75**, pp. 102872.

[11] Serta, C. P. V., Janocha, M. J., Yin, G., and Ong, M. C., 2021. "Numerical simulations of flow-induced vibrations of two rigidly coupled cylinders with uneven diameters in the upper transition Reynolds number regime," *Journal of Fluids and Structures*, **105**, pp. 103332.

[12] Riches, G., Martinuzzi, R., and Morton, C., 2018. "Proper orthogonal decomposition analysis of a circular cylinder undergoing vortex-induced vibrations," *Physics of Fluids*, **30**(10), pp. 105103.

[13] Janocha, M. J., Yin, G., and Ong, M. C., 2021. "Modal Analysis of Wake Behind Stationary and Vibrating Cylinders," *Journal of Offshore Mechanics and Arctic Engineering*, **143**(4), pp. 041902.

[14] Nicoud, F., and Ducros, F., 1999. "Subgrid-scale stress modelling based on the square of the velocity gradient tensor," *Flow, Turbulence and Combustion*, **62**, pp. 183-200.

[15] Weller, H., Tabor G., Jasak, H., and Fureby, C., 1998. "A tensorial approach to computational continuum mechanics using object-oriented techniques," *Computers in Physics*, **12**(6), pp. 620-631.

[16] Prsic, M. A., Ong, M. C., Pettersen, B., and Myrhaug, D., 2014. "Large Eddy Simulations of flow around a smooth circular cylinder in a uniform current in the subcritical flow regime," *Ocean Engineering*, **77**, pp. 61-73.

[17] Tian, G., and Xiao, Z., 2020. "New insight on large-eddy simulation of flow past a circular cylinder at subcritical Reynolds number 3900," *AIP Advances*, **10**, pp. 085321.

[18] Janocha, M.J., Ong, M.C. and Yin, G., 2022. "Large eddy simulations and modal decomposition analysis of flow past a cylinder subject to flow-induced vibration," *Physics of Fluids*, **34**(4), pp. 045119.

[19] Parnaudeau, P., Carlier, J., Heitz, D., and Lamballais, E., 2008. "Experimental and numerical studies of the flow over a circular cylinder at Reynolds number 3900," *Physics of Fluids*, **20**(8), pp. 085101.

[20] Ong, L., and Wallace, J., 1996. "The velocity field of the turbulent very near wake of a circular cylinder," *Experiments in Fluids*, **20**(6), pp. 441-453.

[21] Beaudan, P., and Moin, P., 1994. "Numerical experiments on the flow past a circular cylinder at subcritical Reynolds number," Technical Report No. TF-62. Department of Mechanical Engineering, Stanford University.

[22] Assi, G. R., Bearman, P. W., and Meneghini, J. R., 2010. "On the wake-induced vibration of tandem circular cylinders: the vortex interaction excitation mechanism," *Journal of Fluid Mechanics*, **661**, pp. 365-401.

[23] Morse, T. L., and Williamson, C. H. K., 2009. "Fluid forcing, wake modes, and transitions for a cylinder undergoing controlled oscillations," *Journal of Fluids and Structures*, **25**(4), pp. 697-712.

[24] Lumley, J. L., 1967. "The Structure of Inhomogeneous Turbulent Flows," In: *Yaglom, A. M. and Tartarsky, V. I., Eds., Atmospheric Turbulence and Radio Wave Propagation*, pp. 166-177.

[25] Berkooz, G., Holmes, P., and Lumley, J. L., 1993. "The proper orthogonal decomposition in the analysis of turbulent flows," *Annual Review of Fluid Mechanics*, **25**(1), pp. 539-575.

[26] Serta Fraga, V., Yin, G., and Ong, M. C., 2021. "Three-dimensional numerical simulations and proper orthogonal decomposition analysis of flow over different bottom-mounted ribs," *Ships and Offshore Structures*, **17**(4), pp. 792-827.

[27] Muld, T. W., Efraimsson, G. and Henningson, D. S., 2012. "Mode decomposition on surface-mounted cube," *Flow, Turbulence and Combustion*, **88**(3), pp. 279-310.

[28] Schmid, P.J., 2010. "Dynamic mode decomposition of numerical and experimental data," *Journal of Fluid Mechanics*, **656**, pp. 5-28.

List of Figures

FIGURE 16: Energy and accumulated energy of POD modes on the XY plane; (a) $Ur = 4$; (b) $Ur = 5$; (c) $Ur = 7$.

FIGURE 17: The Energy contribution of the first 20 POD modes on the XY plane; (a) $Ur = 4$; (b) $Ur = 5$; (c) $Ur = 7$.

FIGURE 18: The mode shapes of two leading POD modes: (a, b) $Ur = 4$; (c, d) $Ur = 5$; (e, f) $Ur = 7$.

FIGURE 19: The second harmonic shedding POD modes: (a, b) $Ur = 4$; (c, d) $Ur = 5$; (e, f) $Ur = 7$.

FIGURE 20: The time coefficients and power spectra for the harmonic mode pairs on the XY plane for $Ur = 4$: (a) the first harmonic mode pair; (b) the second harmonic mode pair.

FIGURE 21: The time coefficients and power spectra for the harmonic mode pairs on the XY plane for $Ur = 5$: (a) the first harmonic mode pair; (b) the second harmonic mode pair.

FIGURE 22: The time coefficients and power spectra for the harmonic mode pairs on the XY plane for $Ur = 7$: (a) the first harmonic mode pair; (b) the second harmonic mode pair.

FIGURE 23: Energy and accumulated energy of POD modes for $Ur = 4$ on the YZ planes: (a) $x/D = 0.5$; (b) $x/D = 1$; (c) $x/D = 2$; (d) $x/D = 4$; (e) $x/D = 6$; (f) $x/D = 8$.

FIGURE 24: Energy contribution of the first 20 POD modes for $Ur = 4$ on the YZ planes: (a) $x/D = 0.5$; (b) $x/D = 1$; (c) $x/D = 2$; (d) $x/D = 4$; (e) $x/D = 6$; (f) $x/D = 8$.

FIGURE 25: Energy and accumulated energy of POD modes for $Ur = 5$ on the YZ planes: (a) $x/D = 0.5$; (b) $x/D = 1$; (c) $x/D = 2$; (d) $x/D = 4$; (e) $x/D = 6$; (f) $x/D = 8$.

FIGURE 26: Energy contribution of the first 20 POD modes for $Ur = 5$ on the YZ planes: (a) $x/D = 0.5$; (b) $x/D = 1$; (c) $x/D = 2$; (d) $x/D = 4$; (e) $x/D = 6$; (f) $x/D = 8$.

FIGURE 27: Energy and accumulated energy of POD modes for $Ur = 7$ on the YZ planes: (a) $x/D = 0.5$; (b) $x/D = 1$; (c) $x/D = 2$; (d) $x/D = 4$; (e) $x/D = 6$; (f) $x/D = 8$.

FIGURE 28: Energy contribution of the first 20 POD modes for $Ur = 7$ on the YZ planes: (a) $x/D = 0.5$; (b) $x/D = 1$; (c) $x/D = 2$; (d) $x/D = 4$; (e) $x/D = 6$; (f) $x/D = 8$.

FIGURE 29: The v component of the POD modes at different x locations for $Ur = 4$: (a) Mode 1; (b) Mode 2; (c) Mode 3; (d) Mode 4.

FIGURE 30: The w component of the POD modes at different x locations for $Ur = 4$: (a) Mode 1; (b) Mode 2; (c) Mode 3; (d) Mode 4.

FIGURE 31: The v component of the POD modes at different x locations for $Ur = 5$: (a) Mode 1; (b) Mode 2; (c) Mode 3; (d) Mode 4.

Journal of Offshore Mechanics and Arctic Engineering. Received March 04, 2022;
Accepted manuscript posted June 27, 2022. doi:10.1115/1.4055281

FIGURE 32: The w component of the POD modes at different x locations for $Ur = 5$: (a) Mode 1; (b) Mode 2; (c) Mode 3; (d) Mode 4.

FIGURE 33: The v component of the POD modes at different x locations for $Ur = 7$: (a) Mode 1; (b) Mode 2; (c) Mode 3; (d) Mode 4.

FIGURE 34: The w component of the POD modes at different x locations for $Ur = 7$: (a) Mode 1; (b) Mode 2; (c) Mode 3; (d) Mode 4.